PNAS RESEARCH ARTICLE | PLANT BIOLOGY OPEN ACCESS

# Concerted transport and phosphorylation of diacylglycerol at ER–PM contact sites regulate phospholipid dynamics during stress

Selene Garcia-Hernandez[a], Jorge Morello-López[a], Richard Haslam[b], Vitor Amorim-Silva[a], José Moya-Cuevas[a], Rafael Catalá[c], Louise Michaelson[b], Jessica Pérez-Sancho[a], Vedrana Marković[d], Julio Salinas[c], Johnathan Napier[b], Yvon Jaillais[d], Noemí Ruiz-Lopez[a], and Miguel A. Botella[a,1]

Affiliations are included on p. 11.

Edited by Ralph Bock, Max-Planck-Institut fur molekulare Pflanzenphysiologie, Potsdam-Golm, Germany; received October 17, 2024; accepted April 23, 2025

**A universal response of plants to environmental stresses is the activation of plasma membrane (PM) phospholipase C, which hydrolyzes phosphoinositides to produce soluble inositol phosphate and diacylglycerol (DAG). Because of their conical shape, DAG amounts have to be tightly regulated or they can destabilize membranes. We previously showed that upon stress, Synaptotagmin1 (SYT1) transports DAG from the PM to the endoplasmic reticulum (ER) at ER–PM Contact Sites (CS). Here, we addressed the fate of the incoming DAG in the ER. We show that diacylglycerol kinases (DGKs) DGK1 and DGK2 form a module with SYT1 functionally coupling DAG transport and phosphorylation at ER–PM CS. Although SYT1 and DGK1/DGK2 do not show exclusive ER–PM CS localization, their interaction occurs specifically at ER–PM CS and the removal of ER–PM CS abolishes the interaction. Lipidomic analysis of a *dgk-1dgk2* double mutant supports that DGK1 and DGK2 phosphorylate DAG at the ER and transcriptomic and phenotypic analyses indicate that SYT1 and DGK1/DGK2 are functionally related. Taken together, our results highlight a mechanism at ER–PM CS that coordinates the transfer of DAG from the PM to the ER by SYT1 upon stress and the concomitant phosphorylation of DAG by DGK1 and DGK2 at the ER. These findings underscore the critical role of spatial coordination in lipid metabolism during stress-induced membrane remodeling.**

contact sites | abiotic stress | DAG | PI cycle | signaling

## Significance

Membrane contact sites are nanodomains essential for lipid homeostasis and stress signaling but their specific functions remain poorly understood. Here, we report a spatially coordinated mechanism at endoplasmic reticulum–plasma membrane (ER–PM) contact sites, where Synaptotagmin 1 (SYT1) transports diacylglycerol (DAG) from the PM to the endoplasmic reticulum, where it is subsequently phosphorylated by the interacting diacylglycerol kinases (DGK1/DGK2). This process clears DAG generated by stress-activated phospholipase C (PLC) from the PM and sustains the phosphatidylinositol (PI) cycle, providing insights into plant stress responses and lipid signaling in eukaryotic cells.

Membrane contact sites (MCS) are specialized nanodomains where the membranes of two organelles are at very close apposition without fusion (1, 2). This short distance, usually 10 to 30 nm, is possible due to proteins acting as molecular tethers between the lipid bilayers (3, 4). MCS are a distinctive feature of all eukaryotic cells and are present in almost every organelle, enabling a nonvesicular exchange of lipids, small molecules, and signals and fostering coordinated organelle responses to dynamic environments (5–7).

Most MCS involve contacts of the endoplasmic reticulum (ER) with other organelles, including the plasma membrane (PM) known as ER–PM contact sites (ER–PM CS) (8–10). ER–PM CS play a crucial role in interorganelle communication in plants, mammals, and yeasts. They allow nonvesicular lipid transport (11), regulate calcium homeostasis (12), and contribute to the maintenance of cortical ER morphology (13). Among the proteins involved in tethering at the ER–PM CS are the synaptotagmins (SYTs), in plants, and their counterparts Extended synaptotagmins (E-Syts) and tricalbins (Tcbs), in mammals and yeast respectively. The *Arabidopsis* SYT proteins are characterized by a transmembrane (TM) domain at the N terminus that is embedded in the ER membrane, a SYT-like mitochondrial–lipid binding protein domain (SMP), which harbors lipids in a hydrophobic cavity and is involved in dimer formation (11, 14–16), and two C2 domains at the C-terminus that allow tethering with negatively charged phosphatidylinositol phosphates (phosphoinositides) at the PM (15, 17–19). It has been reported using both confocal microscopy and transmission electron microscopy that SYT1 localizes to the ER and accumulates in specific ER–PM CS in a characteristic "beads-on-a-string" pattern (13, 19).

Environmental stresses trigger the activation of phospholipase C (PLC), which in turn hydrolyzes phosphoinositides into soluble inositol phosphates and diacylglycerols (DAG) at the PM (20, 21). PM-localized diacylglycerol kinases (DGK), such as DGK5, convert DAG into phosphatidic acid (PA), which plays essential signaling roles (22, 23). An excessive accumulation of DAG, due to the conical structure of these molecules, induces negative

Author contributions: S.G.-H., N.R.-L., and M.A.B. designed research; S.G.-H., J.M.-L., V.A.-S., R.C., J.P.-S., and V.M. performed research; J.S., J.N., Y.J., and N.R.-L. contributed new reagents/analytic tools; S.G.-H., R.H., J.M.-C., L.M., and M.A.B. analyzed data; and S.G.-H. and M.A.B. wrote the paper.

The authors declare no competing interest.

This article is a PNAS Direct Submission.



[1]To whom correspondence may be addressed. Email: mabotella@uma.es.

This article contains supporting information online at https://www.pnas.org/lookup/suppl/doi:10.1073/pnas.2421334122/-/DCSupplemental.

Published June 2, 2025.

membrane curvatures leading to destabilization or producing membrane fission and fusion events (24). Therefore, PM DAG concentration must be strictly maintained at very low levels (25). Recently, it has been shown that *Arabidopsis* SYT1 is involved in the transfer of DAG produced by PLC from the PM to the ER (15) and accordingly, the lack of *SYT1* leads to reduced membrane stability during stresses such as salt (19), cold (15), and mechanical damage (18).

The *DGK* family in *Arabidopsis* comprises seven genes (*DGK1-DGK7*) (26). Except for DGK1 and DGK2, which have a transmembrane region (TM) that anchors them to the ER (27), the other proteins lack apparent targeting domains, and therefore, information about their localization is uncertain. So far, it has been shown that DGK4 localizes at the ER membrane based on transient expression in *N. benthamiana* (28) and DGK5 localized at the PM with an essential role in plant immunity (22).

In contrast to plants, human DGKs exhibit a large variety of domains that regulate their activity and membrane targeting (29, 30). Notably, human type III HsDGKε is the only DGK anchored to the ER by a TM, as in DGK1 and DGK2 (31). HsDGKε catalyzes one of the steps of the phosphatidylinositol (PI) cycle, the major metabolic pathway for the synthesis of PI and its phosphorylated forms, the phosphoinositides (32). Therefore, this cycle is essential to replenish the phosphoinositides used by PLC at the PM and to sustain repetitive rounds in response to physiological stimuli. Interestingly, this metabolic cycle is atypical as it occurs in two different cellular compartments, i.e., the ER and the PM, implying that some lipids species must be transferred between these membranes, making ER–PM CS integral participants of this process (33, 34). However, the potential function of SYT1 as part of the PI cycle transporting DAG, the identification of additional components, and how they function at ER–PM CS remains elusive.

The stress-generated DAG at the PM can be either transformed into PA by DGK playing a signaling role (35, 36) or transported to the ER by SYT to maintain PM stability (15) and to replenish the phosphoinositides pool by the PI cycle. Here, we report a mechanism by which DAG is cleared from the PM through the coordinated transport of SYT1, and subsequent phosphorylation by DGK1, and DGK2 at ER–PM CS. We determined their interacting domains, the molecular outcomes of their respective mutants, and investigated the physiological implications in response to cold-acclimated freezing stresses.

Here, we report a spatial coordinated mechanism at ER–PM CS to clear the PM of the DAG generated by stress-activated PLC and to replenish the PIP by the PI cycle. This is achieved by the concerted transport of DAG from the PM to the ER by SYT1, and its subsequent phosphorylation by ER-anchored DGK1 and DGK2, generating a PIP pool readily available at ER–PM CS. This demonstrates that certain proteins can play a role in specific regions, despite being distributed throughout the entire ER. We determined their subcellular localizations, their interacting domains, the molecular outcomes of their respective mutants and investigated the physiological implications in response to stresses, such as cold and freezing.

## Results

**SYT1 Interacts with DGK1 and DGK2.** SYT1 ER–PM tether plays a role in maintaining diacylglycerol (DAG) homeostasis at the PM during abiotic stress (15). To get insight into the function of SYT1, we performed TurboID proximity labeling proteomics in *Arabidopsis thaliana* cell cultures using SYT1 as bait. In addition to previously described SYT1 interactors such as the own SYT1, other SMP containing proteins as SYT4, SYT5, CLB1 (37, 38), and reticulons (39), Diacylglycerol Kinase 1 was also identified (DGK1, AT5G07920) (Fig. 1*A* and *SI Appendix*, Fig. S1). We investigated DGK1 further, as SYT1 and DGKs share a function related to DAG homeostasis and showed that SYT1-RFP coimmunoprecipitates (Co-IP) in *Nicotiana benthamiana* when we use DGK1-GFP as bait (Fig. 1*B*). Next, we performed a structural and phylogenetic analysis of the seven DGK proteins encoded in the *Arabidopsis* genome (40) (Fig. 1*D*) and the ten human DGKs. The *Arabidopsis* DGK family is divided into three clades. DGKs from clade II and III (DGK3-DGK7) comprise a catalytic domain with an ATP-binding site responsible for the phosphorylation of DAG (41), and an accessory domain whose function remains elusive (*SI Appendix*, Fig. S2*A*). The clade I, which includes DGK1 and DGK2, is unique since, in addition to the catalytic and accessory domains, they possess a TM and two C1 domains mediating DAG binding (42) and/or protein–protein interactions (43). DGK1 and DGK2 are structurally and phylogenetically more related to human HsDGKε than other plant DGKs sharing TM-C1x2-catalytic-accessory domains (*SI Appendix*, Fig. S2*A*). Similar to HsDGKε (31), DGK1 and DGK2 localize at the ER based on their colocalization in *N. benthamiana* with the ER marker FaFAH1-RFP, a cytochrome P450 hydroxylase (15) (*SI Appendix*, Fig. S2 *E* and *F*). The main difference between DGK1/DGK2 and HsDGKε is the presence of an Intrinsic Disordered Region (IDR) in DGK1 and DGK2 that is absent in HsDGKε (*SI Appendix*, Fig. S2 *B–D*). Interestingly, all human DGKs possess C1 domains reported to bind DAG and phorbol ester, while DGK1 and DGK2 are the only *Arabidopsis* DGKs carrying these domains (*SI Appendix*, Fig. S2*A*).

Expression of *Arabidopsis DGK* genes in vegetative tissues using RNA sequencing data from eFP SeqBrowser indicated that *DGK1*, *DGK2*, *DGK3*, *DGK5,* and *DGK7* are ubiquitous, whereas *DGK4* and *DGK6* are mainly expressed in pollen (*SI Appendix*, Fig. S3 *A* and *B*). Because of the similar expression pattern of *DGK1* and *DGK2* and their structural similarities, we investigated whether SYT1 could also associate with DGK2. As shown in Fig. 1*B*, DGK2-GFP also coimmunoprecipitated SYT1-RFP, and further analysis showed that DGK1-GFP coimmunoprecipitated DGK2-RFP (Fig. 1*C*), supporting that SYT1, DGK1, and DGK2 likely form a complex.

**Identification of the Interaction Domains of DGK1, DGK2, and SYT1.** To determine whether SYT1, DGK1, and DGK2 directly interact in vivo and to identify their interacting domains, we conducted Förster Resonance Energy Transfer (FRET) analysis using *N. benthamiana* (Fig. 1*E*). Full-length DGK1 (DGK1-GFP), DGK1 lacking the accessory domain (DGK1ΔAcc-GFP), DGK1 containing the TM and the C1 domains (DGK1 C1s-GFP) and SYT1 lacking the C2 domains (SYT1ΔC2AB-GFP) showed bulk ER localization. In contrast, SYT1-GFP showed the typical ER localization enriched at ER–PM CS (Fig. 1*D* and *SI Appendix*, Fig. S4). As a positive control, we used SYT1–SYT1 interaction, and as negative control we used SYT6, another SMP containing ER protein (*SI Appendix*, Fig. S4) that does not interact with SYT1 (17) (Fig. 1*E*). For the FRET analysis, we used proteins tagged at their C termini to the fluorophores GFP and RFP in both directions. FRET experiments showed interaction of SYT1 with SYT1, DGK1, DGK1ΔAcc, and DGK1 C1s (Fig. 1*E*). However, SYT1ΔC2AB did not interact with DGK1-GFP, supporting that the C2 domains of SYT1 interact with the C1 domains of DGK1. To confirm that the interaction of SYT1 occurs through their C2 domain, we performed bimolecular fluorescence complementation (BiFC) assays between SYT1 and SYT1 lacking the C2 domains with DGK2 (Fig. 1*F*). While coexpression of SYT1-cYFP/DGK2-nYFP reconstituted the YFP signal, coexpression of SYT1ΔC2AB-cYFP/DGK2-nYFP did not. As a positive control, we showed

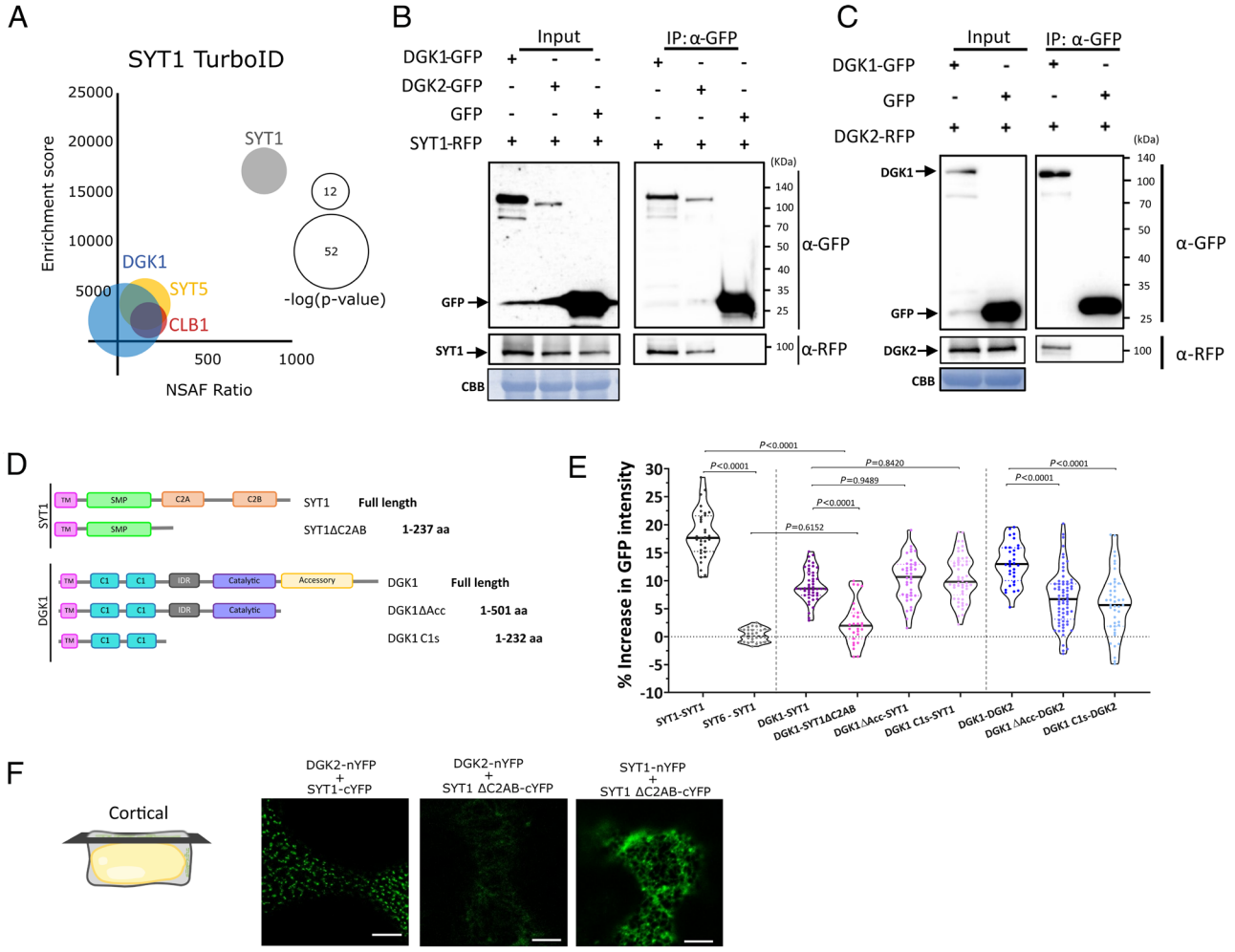


**Fig. 1.** DGK1 and DGK2 interact with SYT1, share a similar structure, and show an ER localization. (*A*) SYT1 TurboID identifies DGK1 as one of the main putative interactors of SYT1, along with SYT5 and CLB1, whose interactions with SYT1 have already been described (37, 38). The bubble plot shows the enrichment score and Normalized Spectral Abundance Factor ratio of each protein. −log(*P*-value) is represented by the circle size. (*B*) A GFP pull-down assay shows that DGK1 and DGK2 coimmunoprecipitate SYT1. Proteins were transiently expressed in *N. benthamiana*, and tissue was harvested 2 d postinfiltration. Proteins tagged with GFP were IP using GFP Trap beads. Total (Input) and IP proteins were separated by SDS-PAGE. DGK2-GFP and DGK1-GFP were detected with a GFP antibody and SYT1-RFP was 1 detected using an anti-RFP antibody. Uniform sample loading was verified by Coomassie blue staining (CBB) on the input samples. (*C*) DGK1 coimmunoprecipitates DGK2. The GFP pull-down assay was performed as in (*A*) using DGK1-GFP and DGK2-RFP. (*D*) Schematic representation of SYT1, DGK1, and their truncated protein versions using in the FRET analysis. DGK1, DGK1ΔAcc, DGK1 C1s, SYT1, and SYT1ΔC2AB were tagged with both RFP and GFP at the C-terminus and all combinations were used in the FRET analysis. (*E*) FRET assays using the full-length and the truncated versions of SYT1, DGK1, and DGK2 (*A*). Protein pairs were coexpressed in N. benthamiana leaves and analyzed at 2 d postinfiltration. The protein pairs shown in the graph are labeled with the first protein fused to GFP and the second fused to RFP. RFP-tagged proteins were photobleached, and the intensity of the GFP-tagged proteins was quantified. The percentage increase in GFP intensity was calculated using the following formula: [(IAfter − IBefore)/IAfter] × 100, where IBefore and IAfter represent the means of the intensity from six measurements taken before and after photobleaching, respectively. The statistical analysis using one-way ANOVA and Tukey multiple comparisons is shown. (*F*) BiFC assay was performed in *N. benthamiana* by coexpressing pairs of proteins. DGK2-nYFP associates with SYT1-cYFP but not with SYT1ΔC2AB-cYFP, indicating a possible role of C2 domains in SYT1–DGK2 interaction. However, SYT1-nYFP is capable of associating with SYT1ΔC2AB-cYFP through the SMP domain. The scheme indicates that the images were taken at the cortical region of lower epidermis cells 2 d postinfiltration. (Scale bar, 10 μm.)

that the coexpression of SYT1-nYFP and SYT1ΔC2AB-cYFP reconstituted YFP fluorescence consistent with their interaction through the SMP domains (15).

Additional FRET analysis indicated an interaction of DGK2 with the full-length DGK1 that was reduced with DGK1ΔAcc and DGK1 C1s-GFP (Fig. 1*E*), supporting that DGK1 and DGK2 proteins mainly interact through their accessory domains. Because all DGKs we have analyzed so far contained an accessory domain (*SI Appendix*, Fig. S2*A*), it is possible that these domains play a role in their localization by the formation of homo- and/or heterodimers.

**SYT1 and DGKs Interact Specifically at ER–PM CS.** The ER can be divided into the bulk ER and the cortical ER (cER). cER corresponds to the ER close to the PM and, therefore, has the competence to form ER–PM CS. Therefore, proteins anchored to the ER can display three potential localization patterns: i) Bulk ER localization, resulting in a reticulated pattern that is characteristic of DGK1 and DGK2 (*SI Appendix*, Fig. S5*A*), ii) Exclusively ER–PM CS localization, which produces a punctate pattern such as the artificial ER–PM tether MAPPER (44) (*SI Appendix*, Fig. S5*B*), and iii) An ER localization with ER–PM CS enrichment, displaying a characteristic "beads and strings" pattern such as SYT1 (18) (*SI Appendix*, Fig. S5*C*). DGK1 and DGK2 showed a bulk ER localization when they were expressed individually (*SI Appendix*, Fig. S4) or coexpressed together (Fig. 2*A* and *SI Appendix*, Fig. S6*A*). However, when coexpressed with SYT1, DGK2 (Fig. 2*A* and *SI Appendix*, Fig. S6*B*) and DGK1 (*SI Appendix*, Fig. S6 *E* and *G*) showed an enrichment at ER–PM CS that did not occur with the ER marker FaFAH-RFP

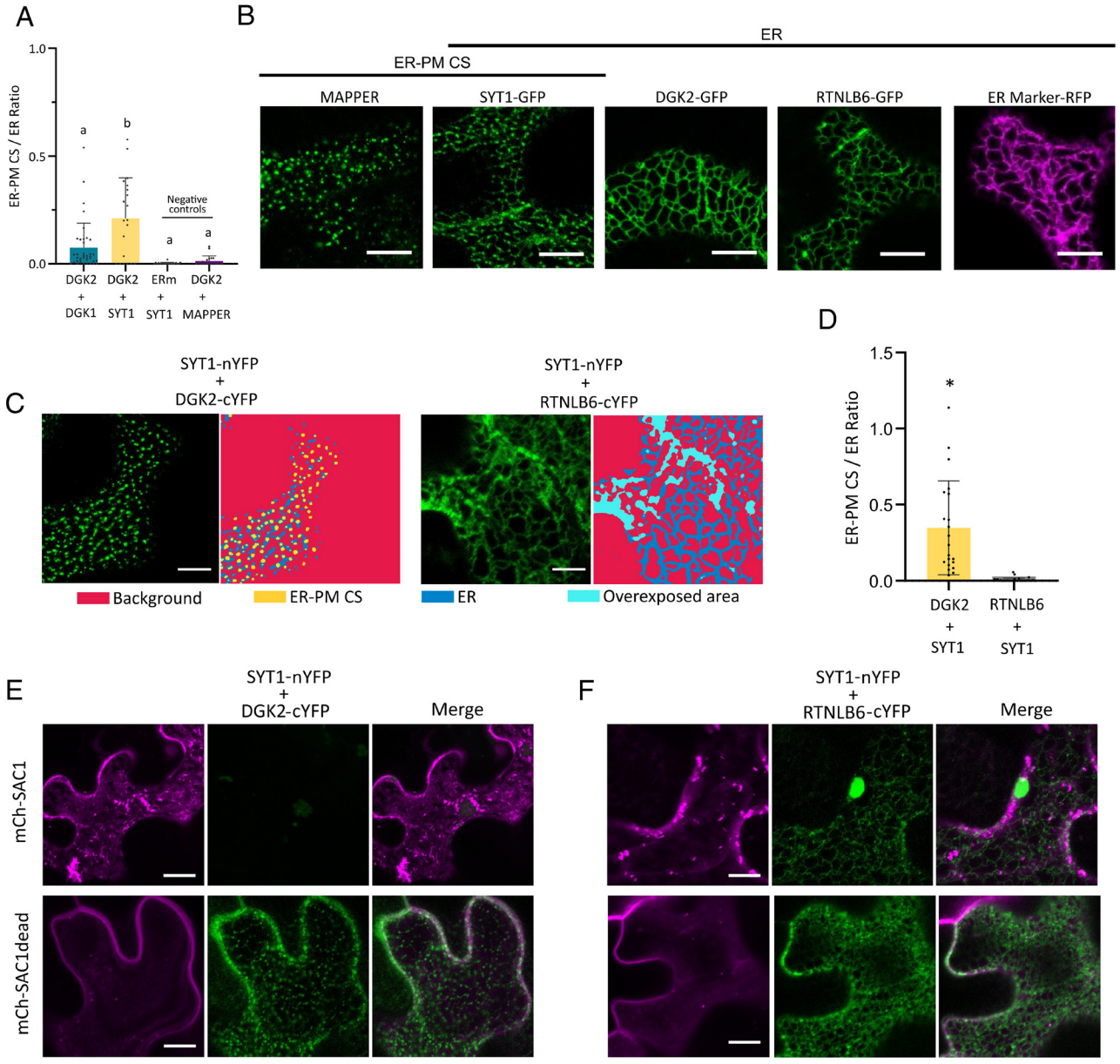


**Fig. 2.** SYT1, DGK1, and DGK2 interact at ER–PM CS. (*A*) The ER–PM CS/ER ratio for DGK1 was quantified in plants coexpressing DGK2 with DGK1, SYT1, and MAPPER, and also for ER marker coexpressed with SYT1. ER–PM CS and ER segmentation was performed as described in (*B*). Error bars indicate SD. Letters indicate statistically significant differences using one-way ANOVA Tukey multiple comparisons, $P < 0.05$ (n > 20). DGK1 increased at the ER–PM CS when coexpressed with SYT1, but not when coexpressed with DGK2 or MAPPER. (*B*) MAPPER, SYT1, DGK2, and RTNLB6 tagged to GFP, and ER Marker-RFP (FaFAH) were infiltrated in *N. benthamiana* leaves. Images were taken 2 d post infiltration at the cortical region of lower epidermal cells. Two types of fluorescence patterns were distinguished: a more punctate pattern corresponding to the ER–PM CS and a more reticular pattern corresponding to the ER. MAPPER is characterized by the punctate pattern, ER marker, DGK2, and RTNLB6 by the reticular pattern, and SYT1 exhibits both of them. (*C* and *D*) The BiFC assay between SYT1-nYFP and DGK2-cYFP shows a punctate pattern, while the assay between SYT1-nYFP and RTNLB6-cYFP displays a reticular pattern. To distinguish between both, several images were segmented using the machine learning tool Ilastik (45) into: Background, ER–PM CS, ER, and overexposed regions where determining ERPM CS is not possible, and thus these regions are excluded from the ratio shown in (*D*). Area of each segmented ROI was measured with FIJI. Error bars indicate SD. Letters indicate statistically significant differences using one-way ANOVA Tukey multiple comparisons, $P < 0.05$ (n > 20). (*E* and *F*) SAC1 is a phosphatase that converts PI4P into PI at the PM. Since PI4P is crucial for the formation of ER–PM CS, SAC1 activity avoids the ER–PM CS formation. Coexpression of SYT1-nYFP/DGK2-cYFP and SYT1-nYFP/RTNLB6-cYFP results in BiFC fluorescence when coinfiltrated with an inactive version of SAC1 (SAC1 dead). However, when coexpressed with the active form of SAC1, SYT1-nYFP/DGK2-cYFP fluorescence disappears, indicating that the interaction of SYT1 and DGK2 depends on ER–PM CS formation.

when coexpressed with SYT1 (Fig. 2*A* and *SI Appendix*, Fig. S6*C*). The localization of DGK1, DGK2, and SYT1 occurs in the same ER–PM CS as shown by the coexpression of SYT1, DGK1, and DGK2 (*SI Appendix*, Fig. S7*A*). This high colocalization also occurs when SYT1 and MAPPER are coexpressed (*SI Appendix*, Fig. S7*B*) as previously shown (44). However, the coexpression of the DGKs with MAPPER did not cause their increase at ER–PM CS (Fig. 2*A*, *SI Appendix*, Fig. S6 *D*, *F*, and *G*). Collectively, these experiments suggest that the enrichment of DGK1 and DGK2 at ER–PM CS depends on their interaction with SYT1 and is not caused by a putative increase in the formation of ER–PM CS.

During the previous BiFC experiments, we noticed that the reconstituted YFP signal highly resembled an ER–PM CS localization pattern such as MAPPER (Fig. 1*F*). When we changed tags and expressed SYT1-nYFP DGK2-cYFP, the BiFC signal also showed a punctuated pattern typical of ER–PM CS proteins (Fig. 2*C*). This is surprising since it differs from SYT1-GFP and DGK2-GFP localizations (Fig. 2*B*) and is consistent with an

interaction of SYT1 and DGK2 specifically at ER–PM CS. This would indicate that the SYT1 interacting domains with DGKs (i.e., the C2s) might require their binding to the PM for the interaction to take place.

If this was the case, the removal of the ER–PM CS should abolish this interaction. To test this hypothesis, we used a PM-anchored MAP-mCherry-SAC1 phosphatase, which depletes PI4P from the PM (46) and was shown to abolish the SYT1 localization at ER–PM CS (15). As a control, we showed that the coexpression of MAP-mCherry-SAC1 changed MAPPER localization from ER–PM CS to bulk ER (*SI Appendix*, Fig. S8 *A* and *B*), while the coexpression of MAPPER with a catalytically inactive MAP-mCherry-SAC1dead did not have any effect (*SI Appendix*, Fig. S8*B*). When we coexpressed SYT1-nYFP and DGK2-cYFP together with MAP-mCherry-SAC1, no GFP signal was detected in any of the cells labeled by mCherry after a thorough analysis (Fig. 2*E* and *SI Appendix*, Fig. S8*D*), which included more than 30 cells per leaf expressing MAP-mCherry-SAC1, 2 leaves per plant, and in 3 plants per replicate. The experiment was conducted three independent times with the same results. However, when we used MAP-mCherry-SAC1dead we detected a YFP signal in ER/PM CS in all mCherry labeled cells (Fig. 2*E* and *SI Appendix*, Fig. S8*D*). To investigate whether this was specific to DGKs and occurred with other SYT1 interactors, we used the reticulon RTNLB6, an ER protein previously shown to interact with SYT1 (39). Like DGK1 and DGK2, RTNLB6-GFP shows a bulk ER localization (Fig. 2*B*), however, the interaction with SYT1 occurs throughout the ER (Fig. 2 *C* and *D*). When we coexpressed SYT1-nYFP and RTNLB6-cYFP, the YFP signal was reconstituted in cells expressing MAP-SAC1-mCherry and MAP-mCherry-SAC1dead, indicating that the interaction of these proteins is not dependent of the formation of ER–PM CS (Fig. 2*F*). To demonstrate that a lack of protein expression was not the cause of the negative interaction, we performed immunoblots using the same leaves analyzed by confocal microscopy and showed that all proteins were expressed (*SI Appendix*, Fig. S8*C*). Next, we performed the BiFC experiment, changing the tags of SYT1 and DGK2 with the same results (*SI Appendix*, Fig. S8 *D* and *E*). Taken together, these results show that the interaction between SYT1 and DGKs occurs specifically at ER–PM CS.

**DGK1 and DGK2 Phosphorylate DAG at the Endoplasmic Reticulum.** The fact that DGK1 and DGK2 are anchored to the ER through TM domains, their interaction with SYT1 at ER–PM CS and the presence of a flexible IDR preceding their catalytic domains (*SI Appendix*, Fig. S2 *C* and *D*) raises the question of whether DGK1 and DGK2 catalyze the phosphorylation of DAG in *cis* in the ER membrane or in *trans* at the PM. Since the phosphorylation of DAG into PA at PM (*trans*) or the ER (*cis*) has distinct functional consequences, determining its specific location activity is important.

To address this, loss-of-function T-DNA mutants for *DGK1* (*dgk1-1*, SALK_053412, *dgk1*) and *DGK2* (*dgk2-2*, SAIL_71_B03, *dgk2*) were obtained and we generated by crossing a *dgk1dgk2* double mutant (*SI Appendix*, Fig. S9*A*) (*Material and Methods*). We performed a lipidomic analysis of harvested leaves of wildtype (WT) and *dgk1dgk2* plants grown in control conditions and after a cold treatment. Cold stress was chosen because it activates PLC and produces the accumulation of DAG at the PM (47), promotes the relocalization of SYT1 at the PM (15), and was the stress that caused the highest accumulation of *DGK1* and *DGK2* transcripts (*SI Appendix*, Fig. S3 *C* and *D*). A two-phase partitioning protocol (15) was used to isolate membrane fractions enriched in either PM or inner membranes (IM, the remaining membranes after two-phase partitioning protocol and PM isolation), primarily consisting of the ER.

After verifying the efficiency of the purification method (*SI Appendix*, Fig. S10), we used liquid chromatography–tandem mass spectrometry (LC-MS; High Resolution/Accurate Mass). Molecular species of DAG, and the abundant phosphatidylcholine (PC) and phosphatidylethanolamine (PE), as well as other relevant lipids present in the fractions, were measured (Fig. 3*A*, *SI Appendix*, Fig. S11, and Dataset S1). The analysis did not reveal differences in the composition in the PM or IM of DAG, PE, or PC between the WT and *dgk1dgk2* under control conditions (Fig. 3*A* and *SI Appendix*, Fig. S11). In cold-treated plants, no differences in DAG, PE, or PC were found in the PM (Fig. 3*A* and *SI Appendix*, Fig. S11). However, a relevant increase in DAG levels (1.6-fold enrichment) (Fig. 3*A*) and a slight increase in PE and PC (1.1 and 1.2-fold, respectively) was obtained in the IM of the *dgk1dgk2* mutant compared to WT (*SI Appendix*, Fig. S11). Single lipid species analysis revealed that most DAG molecular species at the IM displayed a tendency to accumulate in *dgk1dgk2* compared to WT, being DAG34:2 and DAG34:3 the most enriched species (1.8-fold enrichment) (Fig. 3*A*). Additionally, PC34:3 (1.4-fold) and PE34:2 and PE34:3 (1.2-fold) species were also enriched in *dgk1dgk2* compared to WT (*SI Appendix*, Fig. S11). As DAG serves as the substrate for PE and PC biosynthesis at the ER through the CDP-ethanolamine and CDP-choline, the increased levels of these two glycerolipids might indirectly result from the increased abundance of DAG in these plants.

Interestingly, like *dgk1dgk2*, *syt1syt3* double mutant accumulates DAG34:2 and DAG34:3 after cold treatment. This accumulation occurs at the PM, leading to a reduction of the PM integrity (15). In contrast to *syt1syt3*, the PM integrity of *dgk1dgk2* is like WT seedlings, which is consistent with the accumulation of DAG at the ER and not at the PM (Fig. 3 *B* and *C*). These results strongly support that DGK1 and DGK2 function in *cis* by phosphorylating DAG at the ER and therefore are likely playing a role in the PI cycle.

**Molecular and Genetic Relationships between *SYT1* and *DGK1* and *DGK2*.** To determine the effect of cold stress at the molecular level in *syt1* and *dgk1dgk2* relative to WT, we performed a global transcriptome analysis of 2-wk-old seedlings of these genotypes after 24 h at 4 °C. The analysis identified 192 differentially expressed genes (DEG) between WT and *syt1* and 76 DEG between WT and *dgk1dgk2* (Fig. 4*A*), listed in Dataset S2. When we compared DEG between *dgk1dgk2* and *syt1*, we found 24 common genes with a nonrandom overlap (55.2 enrichment with a *P*-value of $9.9^{-36}$). The enrichment was calculated as the number of overlapping genes divided by the expected number of overlapping genes drawn from both groups. Most of the common DEG showed a similar expression trend (*SI Appendix*, Fig. S12), in particular down regulated genes. This overlap of DEG in *dgk1dgk2* and *syt1* strongly supports that *SYT1* and *DGK1*/*DGK2* are functionally related. Functional enrichment analysis of the overlapping DEG for *dgk1dgk2* and *syt1* (Dataset S3) unveiled the highest overrepresentation of GO terms related to abiotic and biotic stress responses (Fig. 4*C*). This is consistent with the described role of *SYT1* in the resistance to various abiotic (15, 17) and biotic stress (48–51).

*SYT1* plays a role in cold-acclimated freezing tolerance (15). Cold acclimation is an adaptive response by which certain plants increase their freezing tolerance after being exposed for some days to low nonfreezing temperatures (52). Therefore, we aimed to determine whether *DGK1* and *DGK2* also play a role in cold-acclimated freezing tolerance. Under standard growth conditions, there were no obvious phenotypic differences in any of the tissues or developmental stages analyzed between the double

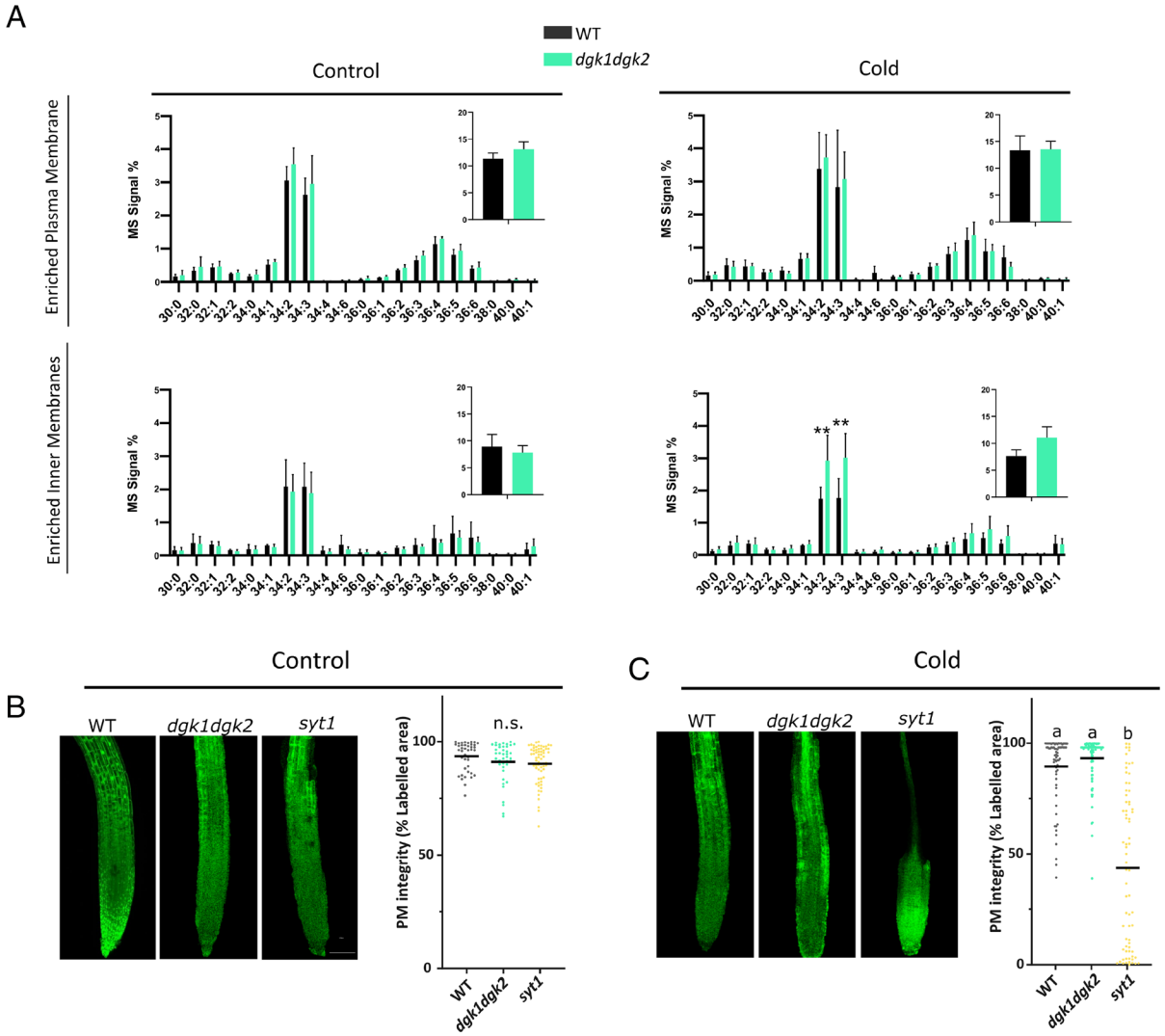


**Fig. 3.** *dgk1dgk2* plants show higher DAG accumulation at the IM than WT plants after cold stress. (*A*) Lipid quantification of the molecular species of DAG in PM and IM using HR/AM. Fractions were isolated from 5-wk-old WT and *dgk1dgk2* rosettes grown at control conditions followed by 3 d of cold treatment (4 °C). PM and IM samples were purified by two-phase partitioning protocol, and lipids were extracted as described in "*Material and Methods*." Acyl chains are expressed as the number of acyl carbons: number of acyl double bonds. Distribution of the identified DAG molecular species in the PM and the IM of WT (black) and *dgk1dgk2* (green) is represented. Column bars show the mean values of at least four biological replicates of MS signal % (pos/neg combined). To avoid polarity switching during a run, each sample replicate was run twice, once each in negative and positive mode. Lipids identified from the two runs were merged into a single, annotated dataset for that replicate. Error bars indicate the SEM. The *Inset* graph represents the sum of all molecular species of the specific lipid. The asterisks indicate statistically significant differences between *dgk1dgk2* and WT as determined by a Dunnett's multiple comparisons test: $^{**}P < 0.0001$; $^{*}P < 0.0002$. (*B* and *C*) Cell viability quantification in 6-d-old *Arabidopsis* roots in control and after cold treatment. Seedlings were cultivated on a solidified 1/10 MS agar medium under long-day photoperiods at 23 °C. Then plants were subjected to a 30 min cold treatment (6 °C in prechilled 1/10 strength liquid MS). Cell viability was assessed using FDA staining, with fluorescence intensity quantified as the percentage of root area exceeding an automatic threshold set by the "Moments" algorithm in Fiji software. Each point represents a measurement from an individual ROI. Horizontal lines indicate the mean values. The experiment was repeated three times with consistent results. Letters indicate significant differences as determined by one-way ANOVA and Tukey's multiple comparisons test.

mutant *dgk1dgk2*, *syt1*, and the triple mutant *dgk1dgk2syt1* (Fig. 4*D*). However, *syt1* and *dgk1dgk2* plants show decreased cold-acclimated freezing tolerance compared to WT plants (Fig. 4 *E* and *F*). The triple *dgk1dgk2syt1* did not show increased sensitivity compared to *syt1*, supporting that they work in a common pathway.

## Discussion

Abiotic stress causes the activation of PLC, leading to the production and transient accumulation of DAG in the PM. However, the stationary amount of DAG at the PM must be maintained at a low level since these molecules exhibit a conical shape within the membrane due to the small polar head, generating regions of negative curvature, inefficient packing, and subsequent instability (24). The DAG at the PM is either converted to the second messenger PA by PM DGKs with a role in signaling (22) or transported to the ER by SYT1 and SYT3 ensuring PM integrity (15). In this work, we show that DGK1 and DGK2 interact with SYT1 specifically at ER–PM CS and exerts its catalytic activity at the ER. This highlights a role of ER–PM CS by allowing the efficient transformation of SYT1-transported DAG at the ER by DGK1 and DGK2 into PA to enhance the PI cycle during stress episodes.

Our analysis reveals that the C2 domains of SYT1 interact with the C1 domains of DGKs. While C1 domains of specific proteins such as PLC are primarily involved in DAG binding (53), they also serve as protein-interacting modules. For example, the C1 domains of DGKζ binds Rac1 (54) and β-arrestins (55). Since DGK1 and DGK2 are the only *Arabidopsis* DGKs containing C1 domains (*SI Appendix*, Fig. S2*A*), it is unlikely that any other

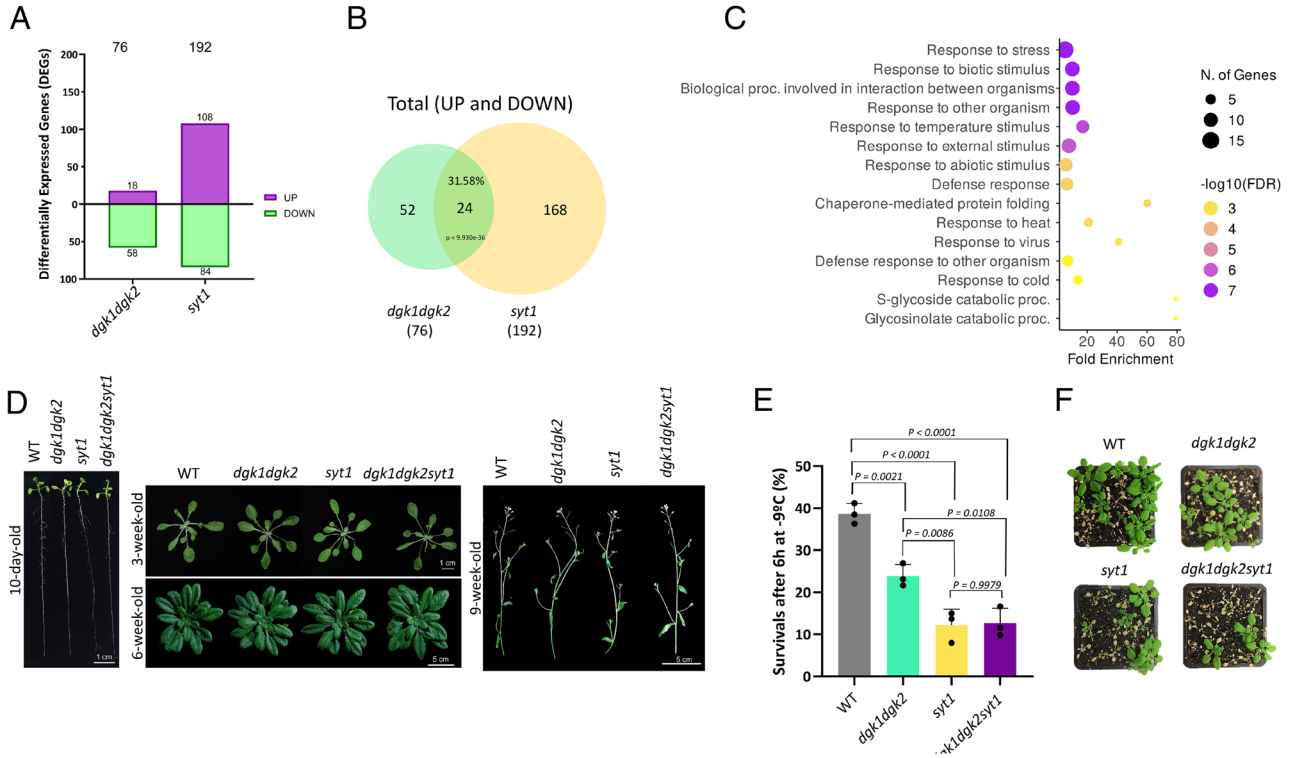


**Fig. 4.** Global transcriptomic analyses indicate that *SYT1* and *DGK1*/*DGK2* regulate similar genes. RNAseq analysis was performed using the aerial parts of a pool of 2-wk-old plants (approximately 10 plants per biological replicate and at least three replicates per group) grown in soil under control conditions and subsequently cold-treated (4 °C) during 24 h. (*A*) Number of DEGs (q-value < 0.05) in *dgk1dgk2* and *syt1* compared to the WT. Up-regulated genes are represented in purple and down-regulated in green. (*B*) Venn diagram of DEGs in *dgk1dgk2* and *syt1* and their overlap. The percentage of shared genes are calculated relative to the number of total DEGs in the *dgk1dgk2* mutant. The enrichment of the overlap is 55.2 and is calculated as the number of overlapping genes divided by the expected number of overlapping genes drawn from two independent groups. The expected genes are defined by the following formula: (no. of genes in *dgk1dgk2* × no. of genes in *syt1*)/total genes analyzed in the whole genome. *P*-value of the enrichment is indicated. (*C*) Bubble plot of the GO terms from the 24 overlapping genes in panel (*B*). The fold enrichment of each category is shown on the X axis, while the FDR is represented by a color gradation from purple, lowest, to yellow, highest. The circle size corresponds to the number of genes involved in each GO term. Most of these GO terms are related abiotic and biotic stress responses. (*D*) WT, *dgk1dgk2*, *syt1*, and *dgk1dgk2syt1* do not exhibit obvious phenotype differences when grown in standard conditions. Images show: 10-d-old seedlings grown on vertical plates; Rosettes of 3 and 5 wk grown in soil; and Internodes of 7-wk-old plants. Scale is indicated in the figure. (*E* and *F*) DGK1DGK2 and SYT1 are implicated in the same pathway related to freezing tolerance. Surviving plants of acclimated WT, *dgk1dgk2*, *syt1*, and *dgk1dgk2syt1* after a freezing treatment 6 h at −9 °C and 1 wk of recovery under control conditions. Data represent mean ± SD (n > 20 plants per replicate) using one-way ANOVA and Tukey multiple comparisons.

DGKs will interact with SYT1, however, the finding that DGK1 and DGK2 form heterodimers through their accessory domains opens the possibility that other kinases could also be part of the complex. In addition, these findings could have significant implications for general DGK function since accessory domains are present in all DGKs, we have analyzed.

The TM domain regulates HsDGKε activity by causing a conformational change that brings the active site closer to the membrane (56). Interestingly, the activity of HsDGKε is regulated by negative membrane curvature and shows low activity in flat membranes (57). Whether DGK1 and DGK2 exhibit similar curvature-dependent activity has yet to be established, but if this was the case, a negative membrane curvature caused by the local accumulation of DAG transported by SYT1 at ER–PM CS could regulate DGK1/DGK2 activity. Interestingly, in tissues with endogenous expression, HsDGKε localizes at ER–PM CS, such as the subsurface cisterns of Purkinje cells in rat brains (32, 58). Therefore, it is tempting to speculate that, as we have shown in plants, HsDGKε could form a module with the Extended Synaptotagmins (the SYT1 homologs) to regulate DAG homeostasis in mammals at ER–PM CS, having important functional implications beyond plants.

Sustained production of inositol phosphates (InsP) and DAG during stress responses requires a continuous PI delivery from its synthesis site in the ER to the PM to maintain PIP levels (59). In addition, DAG and PA products generated at the PM must be recycled back to the ER as part of the PI cycle, which is a sequence of enzymatic reactions central to many cellular functions, including cell growth, stress resistance, cytoskeletal organization, and vesicular trafficking (5, 60). Since phosphoinositides are produced in the PM, and PI is synthesized in the ER, lipid transfer events between the ER and PM must occur, establishing the ER–PM CS as a fundamental component of this process.

The interaction between SYT1, DGK1, and DGK2, together with their role in DAG homeostasis, implies an interrelated function. The outcome of the transcriptomic analysis strongly reinforces this interdependency, which is somewhat surprising because *syt1* and *dgk1dgk2* mutations cause the accumulation of DAG in different membranes, i.e., PM vs. ER. Therefore, it is likely that the outcome is caused by a faulty PI cycle leading to defective signaling under episodes of continuous stress. This is reinforced by 1) the Gene Ontology of the overlapping DEGs in these mutants that revealed their implication in stress responses (Fig. 4*C*) and 2) the function of conditions, *SYT1* and *DGK1*/*DGK2* in cold-acclimated freezing tolerance, with the genetic analysis indicating that these genes function in the same pathway (Fig. 4*D*).

Understanding the cellular membrane where DGKs exert their function is critical for comprehending the DAG pool used by these enzymes and their role in DAG metabolism. The lipidomic

analysis of *dgk1dgk2* indicates a cold-stress accumulation of DAG at the ER, supporting a cis-function of DGK1 and DGK2 at the ER, as previously suggested for DGK2 and DGK4 (28). This supports a dynamic interplay between DGK1, DGK2, and SYT1, where the stress-generated DAG is transported from the PM to the ER by SYT1 at ER–PM CS and later transformed into PA by action of DGK1 and DGK2. This interplay is further supported by the fact that two of the most abundant DAG species (34:2, 34:3) that accumulated at the PM of the *syt1syt3* mutant (15) are also the primary species accumulated in *dgk1dgk2* ER membranes. This is further reinforced by the finding that the plant SYT ortholog E-Syt1 accumulates at ER–PM CS following G-protein-coupled receptor-mediated activation of PLC (11, 61, 62) and the identification of HsDGKε at ER–PM CS as the enzyme catalyzing one of the steps in the PI cycle at ER–PM CS (56). In animals, PI is transferred to PM by TMEM24, an SMP-containing protein localized at ER–PM CS (63–65). PI is also transported from the ER to the PM by Nir2, which is also required to transfer PA from the PM to the ER (5, 66). In plants, no orthologs of Nir2 or TMEM24 have been described, and the subcellular localization of CDP-DAG and PIS involved in PI formation is not fully established, although PIS has been observed in the ER (67). Likely, an unreported ER–PM CS localized protein transfers this PI from the ER to the PM.

In summary, our work -based on protein–protein interaction studies, localization characterization by confocal microscopy, lipidomics, transcriptomics, and phenotypic characterization- describes the mechanism by which DAG produced by stress-activated PLC is removed from the PM by the combined action of SYT1, DGK1, and DGK2. While our previous study demonstrated that SYT1 transports DAG from the PM to the ER to prevent its accumulation and potential damage to the PM (15), the subsequent fate of DAG within the ER remained unclear. Here, we uncover that the DAG transferred from the PM to the ER by SYT1 is used by DGK1 and DGK2 to generate PA. This process not only facilitates DAG clearance from the PM, but also enhances the efficiency of the PI cycle, which depends on both the PM and ER, making the ER–PM CS an ideal location for these reactions. Of particular interest is the finding that SYT1, DGK1, and DGK2 interact specifically at ER–PM CS, although DGK1 and DGK2 show a bulk ER localization. A possible mechanistic explanation is that the C2s of SYT1 only interact with DGK1 and DGK2 when contacting the PM by acquiring a different conformation. This is relevant because proteins that show a general ER localization could function specifically at ER–PM CS through interaction with ER–PM components, as we have shown for SYT1 and DGKs. Future challenges will be the identification of additional components in plants involved in the PI cycle and determining their role at ER–PM CS.

## Materials and Methods

**Plant Material.** We used *A. thaliana* (Col-0 ecotype) and *N. benthamiana* as experimental materials. *Arabidopsis* mutant lines used in this study are *syt1* (AT2G20990) SAIL_775_A08, previously characterized by Pérez-Sancho et al. (18); *dgk1-1* (AT5G07920) SALK_053412, and *dgk2-2* (AT5G63770) SAIL_71_B03, both obtained from The European *Arabidopsis* Stock Center (NASC: http://arabidopsis.info/) (*SI Appendix*, Fig. S9*A*). The presence of the T-DNA insert in each mutant was confirmed using diagnostic PCR (*SI Appendix*, Fig. S9*B*), employing allele-specific primers as listed in Dataset S4. This procedure ensured the identification of homozygous plants carrying the insertion and no *DGK1* or *DGK2* transcripts were detected by RT-PCR (*SI Appendix*, Fig. S9*C*). These lines are expected to be null mutants because the T-DNAs disrupt the catalytic domains of DGK1 and DGK2 (*SI Appendix*, Fig. S9*D*). The *dgk1dgk2* double mutant was generated by crossing *dgk1-1* and *dgk2-2*. *dgk1dgk2* was also crossed with *syt1* to generate the triple mutant *dgk1dgk2syt1*. All *Arabidopsis* lines are summarized in Dataset S5.

**Plant Manipulation and Growth Conditions.** *Arabidopsis* seeds were surface sterilized with chlorine vapors (100 mL bleach + 3 mL 37% HCl) in a sealed container for 4 h, then air-cleared for at least 2 h in a laminar flow cabinet. Seeds were plated under sterile conditions on ½ Murashige–Skoog medium with 1.5% (w/v) sucrose and 0.8% (w/v) agar. Plated seeds underwent 3-d vernalization at 4 °C in darkness, then grew vertically in a chamber (16 h light/8 h dark, 130 ± 30 μmol photons $m^{-2}$ $s^{-1}$, 22 ± 1 °C). After 7 d in vitro, seedlings were either collected for analysis or transferred to soil (organic substrate:vermiculite, 4:1 v/v) under the same conditions. Plants were watered every 2 d. For seed collection, plants were dried and stored under low humidity; freshly harvested seeds were used for phenotypic analysis.

**Plasmid Constructs.** Genomic DNA and cDNA from *Arabidopsis* Col-0 were used to amplify target gene promoters and Coding DNA Sequences (CDS) with high-fidelity DNA polymerase (iProof, BioRad #1725301) and primers (Dataset S4). Using Multisite Gateway cloning, the DGK1 (2,472 bp) and DGK2 (1,438 bp) promoter regions were inserted into pDONR R4-L1 via BP reactions (Invitrogen), forming pENTR R4-promoter-L1 constructs alongside pENTR L4-proCaMV35S-R1 (68) and pENTR L4-UBQ10-R1 (69). CDS fragments (DGK1, DGK2, SYT6, RTNLB6) were cloned into pDONR L1-L2, generating pENTR L1-CDS-L2 constructs. Truncated versions of DGK1 (DGK1ΔAcc, DGK1-TM-C1) and SYT1 (SYT1ΔC2AB) were cloned similarly. All constructs were verified by PCR, restriction analysis, and sequencing. For expression plasmids, pENTR L4-promoter-R1, pENTR L1-CDS-L2, and pENTR R2-tag STOP codon-L3 (GFP, RFP, or BFP) (68) were combined with pDestination (pDEST) vectors (pGWB5, pH7m34GW, pDEST GW-cYFP, pDEST GW-nYFP) via LR reactions (Invitrogen) (Dataset S6). The resulting constructs included UBQ10:DGK2-RFP, 35S:DGK2-GFP, UBQ10:DGK1-RFP, 35S:DGK1-GFP, and various truncated and tagged versions of DGK1, SYT1, and RTNLB6, used for transient expression in *N. benthamiana*. Previously described constructs (35S:SYT1-GFP, UBQ10:SYT1-RFP, 35S:GFP, SYT1:MAPPER; 15) were included. Additionally, the pENTR-FaFAH1 CDS vector (70) was provided by Iraida Amaya and inserted into pDEST pGWB5 to create 35S:FaFAH1-GFP. The Pro35::SYT1-TurboID construct was generated as described in the "*Turbo-ID-Based PL*" section.

**Turbo-ID-Based PL.** For the Turbo-ID SYT1 construct, the ORFs of SYT1 flanked by the C and D Greengate cloning overhangs and BsaI sites were synthetized by GenScript and cloned into pUC57-Km vector. Upstream of SYT1 ORF we included the BsaI site plus C Greengate cloning overhangs: AGAAGTGAAGCTTGGTCTCAGGCTCC. Downstream of SYT1 we included BsaI site plus D Greengate cloning overhangs: TCAGTGAGACCGAATTCTCGCCCT. For the synthesis, an internal BsaI site was removed without altering the amino acid sequence and the stop codon was not included to allow the C-terminal tag fusion of the TurboID sequence in the expression vector. To obtain the final expression vector Pro35S::SYT1-TurboID, we used Golden Gate assembling with the Green Gate method previously described (71). The TurboID analysis was performed using *Arabidopsis* cell suspension cultures transformed with Pro35::SYT1-TurboID construct by the Interactomics Facility of the VIB department PLant Systems Biology as previously described (72), using denaturing extraction buffer [100 mM Tris (pH 7.5), 2% (w/v) SDS, 8 M urea] and with the additional acid elution step following the trypsin/Lys-C digest.

***Arabidopsis* eFP Browser Data Analysis.** Expression levels of the 7 DGK genes present in *Arabidopsis* across various tissues and stages were extracted from the available RNA-seq data in the eFP-Seq Browser website (https://bar.utoronto.ca/eFP-Seq_Browser/) (73).

18-d-old wild-type (WT) seedlings, grown under long-day photoperiod, 24 °C, and 50% humidity conditions, were subjected to various abiotic stresses. The shoot outcomes of this assay were acquired from the *Arabidopsis* eFP Browser (http://bar.utoronto.ca/efp/cgi-bin/efpWeb.cgi) (74). Differential expression was determined by dividing the gene's expression value under a specific abiotic stress condition by its corresponding control value, yielding the fold change of abiotic stress compared to the mock condition.

**In Silico Structural Data Analysis.** Domain prediction was conducted using the InterPro tool (https://www.ebi.ac.uk/interpro/) (75). AlphaFold (https://alphafold.ebi.ac.uk/) (76, 77) was used to predict the tertiary structure of DGK1, DGK2, and HsDGKε. The IDR domain of DGK1 and DGK2 was predicted using the program IUPRED3 (https://iupred3.elte.hu/plot). Prion-like residues of DGK1 and DGK2 were obtained using the PLAAC online tool with the defective values, i.e., core length of 60 and relative weight of 100. Protein regions were considered disordered if they had a MobiDB consensus score above 0.15 (15% disordered residues) and prion-like if they contained a prion-domain (≥60 amino acids).

**Transient Expression in *N. benthamiana*.** Different constructs were transformed into *Agrobacterium tumefaciens* (GV3101::pMP90) by electroporation, including p19 to prevent gene silencing. *A. tumefaciens* strains were grown overnight at 28 °C in LB medium with rifampicin (50 μg/mL), gentamicin (25 μg/mL), and the construct-specific antibiotic (spectinomycin 100 μg/mL or kanamycin 50 μg/mL). Cultures were centrifuged (3,000 × g, 15 min, RT), and pellets were resuspended in agroinfiltration solution (10 mM MES pH 5.6, 10 mM $MgCl_2$, 1 mM acetosyringone), then incubated in the dark for 2 h at room temperature (RT). For single-gene expression, Agrobacterium suspensions were mixed to reach $OD_{600}$ of 0.70 for the construct and 0.25 for p19; for double infiltrations, $OD_{600}$ was 0.40 for constructs and 0.15 for p19. Two leaves from 3-wk-old *N. benthamiana* plants (3rd and 4th from the apex) were infiltrated on the abaxial side using a needleless 1 mL syringe. Plants were maintained under growth conditions for 2 d before confocal microscopy analysis and, if applicable, sample collection.

**Confocal Microscopy Images.** For confocal imaging, *N. benthamiana* leaves were infiltrated as described in "*Transient Expression in N. benthamiana*". Leaf disks were excised from the plants immediately before visualization. GFP, RFP, or YFP fluorescence of the lower epidermis was visualized 2 d postinfiltration by confocal microscopy. Confocal images were captured using the Zeiss LSM880 confocal microscope. The GFP and YFP excitations were achieved using the 488 nm argon laser, while the 561 nm laser was utilized for the RFP excitation. For colocalization, sequential line scanning mode was used to separate signals. Fluorophores detection involved a PMT, a GaAsp (used to improve signal recognition), and an additional PMT for transmitted light. Objectives employed were Plan-Apochromat 40× (water) and 63× (oil) with up to 4× digital zoom. Cortical plane images are a maximum Z projection of several planes (900 nm spacing) from the cell surface to the cell interior. The equatorial images used in the FRET assay correspond to single-plane images. Microscopy image processing was performed using the program FIJI (78). Root damage was quantified by assessing the percentage of the root area exhibiting visible FDA fluorescence above a predefined threshold, as previously described (15).

**BiFC Constructs for Expression in *N. benthamiana*.** For BiFC assay, full-length cDNA of *DGK2* and *SYT1* were cloned into the pDEST-GW-nYFP and pDEST-GW-cYFP vectors (79). Each vector contains one-half of YFP fused to the C-terminal of the target proteins (DGK2-nYFP and SYT1-cYFP). 35S:DGK2-nYFP and 35S:SYT1-cYFP expression vectors were transformed into *Agrobacterium* and infiltrated in *N. benthamiana* as detailed in the "*Transient Expression in N. benthamiana*" section. Subsequently, the interaction between DGK2 and SYT1 was observed detecting, by confocal microscopy, the fluorescence produced by the binding of nYFP and cYFP, as described in "Confocal microscopy images." As negative control we used the full-length 35S:DGK2-nYFP coinfiltrated with 35S:SYT1ΔC2AB-cYFP, that did not produce fluorescence. We also check the ability of 35S:SYT1ΔC2AB-cYFP of interacting with other proteins by coexpressing with 35S:SYT1-nYFP. Additionally, we analyzed the fluorescence pattern produced by the association of 35S:SYT1-nYFP with 35S:DGK2-cYFP and with 35S:RTNLB6-cYFP.

**FRET Analysis.** Three-week-old *N. benthamiana* leaves transiently coexpressing N-terminal GFP- and RFP-tagged proteins were used for FRET analyses. Single-plane confocal images were captured using a Zeiss LSM880 confocal microscope with a Plan-Apochromat 40×/1.2 NA (water) objective lens. Equatorial sections of lower epidermal cells with similar colocalized protein intensity were examined. Three regions of interest (ROI) were measured: ROI 1 was photobleached over the acceptor fluorophore (RFP) using a 561 nm laser for 100 iterations at 100% power; ROI 2 was a randomly selected nonphotobleached area; ROI 3 was a background area with no signal. Six donor fluorophore (GFP) measurements were taken per ROI before (Pre) and after (Post) photobleaching. FRET efficiency, calculated as the percentage increase in donor intensity (% ΔGFP) after acceptor removal, followed the formula: % ΔGFP = 100 × (Post − Pre)/Post (80). ROI 2 and 3 served as technical controls, showing no GFP intensity increase, while ROI 1 data determined interactions. Over 25 measurements were taken across different cells, leaves, and plants for each protein pair, with three independent experiments yielding similar results.

**ER–PM CS and ER Segmentation and Quantification.** Confocal images of the cortical plane of transiently coexpressed proteins in *N. benthamiana* leaves were segmented in ER and ER–PM CS in a semiautomatic way, using the interactive machine learning tool ilastik (45). First, the program was trained to distinguish between ER, ER–PM CS, background and overexposed areas where it is not possible to distinguish ER–PM CS because is already saturated. For this purpose, images of SYT1, MAPPER, DGK1, and DGK2 individually infiltrated were used, and structures that were humanly defined as ER (lines forming a network) or as ER–PM CS (dots at the vertices of the ER network) were drawn, distinguishing from each other. After the training process, ilastik segmented the study images, and the areas corresponding to ER and ER–PM CS were quantified in FIJI. The ratio ER–PM CS/ER was calculated for each ROI.

**Protein Extraction and Immunoblot Analysis.** *Arabidopsis* or Nicotiana tissue was ground to a fine powder in liquid nitrogen. Proteins were extracted by incubating 100 mg of sample with Laemmli 2× buffer (125 mM Tris-HCl pH 6.8, 4% SDS, 20% glycerol, 2% β-mercaptoethanol, 0.01% bromophenol blue) at 75 °C for 30 min, then centrifuged (20,000 × g, 1 min, RT) to collect supernatants. Proteins were separated by SDS-PAGE and electrotransferred onto a PVDF membrane (Immobilon-P, Millipore, 0.45 μm, IPVH00010). The membrane was blocked with 5% milk in TTBS (2 h, RT), then incubated overnight at 4 °C with TTBS 1% milk and primary antibodies: anti-GFP 1:600 (Santa Cruz, sc-9996), anti-RFP 1:2,000 (ChromoTek, 6g6), anti-HA 1:2,000 (Sigma, H3663), anti-c-MYC 1:1,000 (GeneScript, A00704), anti-SYT1 1:5,000 (rabbit polyclonal), anti-AHA3 1:10,000 (gift from Ramón Serrano, IBMPC, Valencia, Spain), anti-BIP 1:2,500 (Agrisera, AS09 481), anti-V-ATPase 1:2,000 (Agrisera, AS07 213), anti-TOC75-3 1:2,000 (Agrisera, AS08 351). After washing, membranes were incubated (2 h, RT) with HRP-conjugated secondary antibodies: anti-mouse 1:80,000 (Sigma, A9044) or anti-rabbit 1:80,000 (Sigma, A0545). Detection was performed using ChemiDoc XRS+ (BioRad) with Clarity Western ECL (BioRad, 170-5060) or SuperSignal West Atto (Thermo, A38555). Exposure times ranged from a few seconds to 10 min, and only nonsaturated images were used for quantification in FIJI (78). After immunodetection, membranes were stained with Coomassie R-250 to confirm uniform loading.

**Co-IP Assay.** Co-IP experiments followed Amorim-Silva et al. (81) with slight modifications. *N. benthamiana* leaves (3-wk-old, transiently transformed) were ground, and proteins were extracted from 0.5 g of tissue by incubating the powder for 30 min on an end-over-end rocker at 4 °C with 1 mL of nondenaturing extraction buffer (50 mM Tris–HCl pH 7.5, 150 mM NaCl, 1% Nonidet P-40, 10 mM EDTA, 1 mM $Na_2MoO_4$, 1 mM NaF, 10 mM DTT, 0.5 mM PMSF, 1% protease inhibitor [Sigma, P9599]). Extracts were centrifuged (15,000 × g, 20 min, 4 °C) and filtered through Poly-Prep chromatography columns (Bio-Rad, 731-1550). A 100 μL aliquot was saved as input for Western blot, while the remainder was incubated for 2 h with 30 μL GFP-fused protein agarose beads (Chromotek). To prevent unspecific binding, Nonidet P-40 concentration was adjusted to 0.2% during incubation, as recommended by the manufacturer. Beads were washed four times with detergent-free extraction buffer, resuspended in 75 μL of 2× Laemmli Buffer, and heated at 75 °C for 30 min to dissociate immunocomplexes. Proteins were analyzed as described in the "*Protein Extraction and Immunoblot Analysis*" section, running input and immunoprecipitated (IP) samples in duplicate SDS-PAGE gels for GFP and RFP detection. Co-IP assays were performed twice with consistent results.

**Phylogenetic Analysis.** The protein sequences of all human and *Arabidopsis* DGKs were obtained from the UniProt database (https://www.uniprot.org/), and the alignment was done by Clustal W (https://www.ebi.ac.uk/Tools/msa/clustalo/) and phylogenetic analyses were conducted using the software MEGA X (82). The evolutionary history was inferred using the Maximum Likelihood method and JTT matrix-based model. The bootstrap consensus tree inferred from 500 replicates represents the evolutionary history of the taxa analyzed. Branches corresponding to partitions reproduced in less than 50% bootstrap replicates are collapsed. The percentage of replicate trees in which the associated taxa clustered together in the

bootstrap test (500 replicates) is shown next to the branches. The initial tree for the heuristic search was obtained automatically by applying Neighbor–Join and BioNJ algorithms to a matrix of pairwise distances estimated using a JTT model, then selecting the topology with superior log likelihood value. This analysis involved 17 amino acid sequences, and there were a total of 344 positions in the final dataset.

**RNA Extraction for RT-PCR and RNASequencing (RNAseq).** Total RNA was extracted using the E.Z.N.A Plant RNA kit (BIO-TEK, R6827-01) following the manufacturer's instructions from 50 mg of tissue ground in liquid nitrogen. Genomic DNA was removed with RNase-free DNase I (Omega BIO-TEK, E1091). RNA purity, integrity, and concentration were assessed using Nanodrop One and agarose gel electrophoresis. For RT-PCR, 10-d-old seedlings grown on plates were used. 500 ng of RNA was reverse transcribed into cDNA using iScript reverse transcriptase (BioRad, 1708890). The absence of genomic DNA and successful cDNA synthesis were confirmed via LOX2 diagnostic PCR, where LOX2 was only amplified in cDNA, not RNA samples. RT-PCR using specific primers (Dataset S4) confirmed that T-DNA insertions in *dgk1-1* and *dgk2-2* mutants disrupted transcription. For RNAseq, aerial parts of 2-wk-old seedlings (10 per biological replicate, three replicates per group) grown in soil under control conditions were collected after 24 h cold treatment (4 °C).

**RNAseq Bioinformatic Analysis.** The clustering of the index-coded samples was performed on a cBot Cluster Generation System using the TruSeq PE Cluster Kit v3-cBot-HS (Illumina) according to the manufacturer's instructions. After cluster generation, the library preparations were sequenced on an Illumina Novaseq platform, and 150 bp paired-end reads were generated at the Novogene (UK) Company Ltd. At last, RNA integrity was assessed using the RNA Nano 6000 Assay Kit of the Bioanalyzer 2100 system (Agilent Technologies, CA). The reads were quality-filtered and trimmed using Trimmomatic version 0.36 (83) with default paired-end mode options. The resulting reads were then aligned to the TAIR10 version of the *Arabidopsis thaliana* genome sequence (https://www.arabidopsis.org/) using Hisat2 version 2.1.0 (84). These read alignments (in BAM format) were used for transcript quantification with the cuffdiff program of the Cufflinks version 2.2.1 package (85). The resulting read alignments were visualized and clustered using Tablet software (86) and CummeRbund R package version 2.23.0 (87). To determine DEGs, a false discovery rate (FDR) (q-value) cutoff of ≤ 0.05 was set. DEGs were subjected to singular enrichment analysis for the identification of overrepresented GO terms using PANTHER (88) with the default options (Fisher's Exact as the test type and the Bonferroni correction for multiple testing, $P < 0.05$). The RNA seq raw data from this manuscript are publicly available in Gene Expression Omnibus (GEO; https://www.ncbi.nlm.nih.gov/geo/) under the identifier SUB15096052. The resulting FPKM and DEGs data are in Dataset S2.

**PM and IM Isolation.** For membrane isolation, WT and *dgk1dgk2 Arabidopsis* plants were grown vertically on plates under a short-day photoperiod for 7 d, then transferred to soil for 1 wk before switching to a long-day photoperiod for 3 wk. Before bolting, plants underwent a 3-d cold treatment at 4 °C. Aerial parts were harvested for PM and IM isolation, following Bernfur et al. (89) with modifications. Five grams of 5-wk-old leaves were homogenized in 35 mL of buffer [330 mM sucrose, 50 mM MOPS-KOH pH 7.5, 5 mM EDTA, 5 mM EGTA, 20 mM NaF, 5 mM ascorbate, 5 mM DTT, 150 μM Protease Inhibitor (Pefabloc, 11429868001), 0.6% (w/v) PVPP], with DTT and inhibitors added just before use. Steps were performed at 4 °C to prevent degradation. The homogenate was filtered through 4 layers of nylon mesh (200 μm) and centrifuged at 10,000 g for 15 min to remove debris (broken cell walls, large membrane fragments), nuclei, chloroplasts (intact or fragmented), mitochondria, and any unbroken cells or large aggregates (if present). The resulting total fraction was centrifuged at 100,000 g for 2 h at 4 °C. The supernatant was discarded, and the microsomal pellet was resuspended in buffer (0.33 M sucrose, 5 mM K-phosphate pH 7.8, 0.1 mM EDTA, 1 mM DTT) to 6 g. The two-phase partitioning system had 6.1% (w/w) Dextran T500, 6.1% (w/w) PEG 3350, 330 mM sucrose, 5 mM K-phosphate pH 7.8, 3 mM KCl, and water up to 9 g. Two systems had 3 g of the microsomal fraction, and two had 3 g of buffer. Following Larsson et al. (90), PM and IM phases were obtained, combined, diluted 3× in buffer, and centrifuged at 100,000 g for 2 h at 4 °C. The PM pellet was resuspended in 100 μL of buffer with 5 mM KCl, and the IM pellet in 1 mL. Samples were stored at −80 °C until lipid extraction.

**Lipid Extraction and Analysis.** Lipids were extracted from 100 μL of PM or IM. Glassware was used throughout the procedure. The samples and 1 mL of isopropanol were incubated at 75 °C for 20 min. Subsequently, 2 mL of chloroform/methanol (1:1) and 0.7 mL of water were added. After 30 s of vortex, 2 mL of chloroform/water (1:1) was added. The mixture was centrifuged for 3 min at 500 g, and the lower chloroform phase was gently transferred to a new tube. A re-extraction of lipids was performed by adding 1 mL of chloroform to the first tube, repeating the centrifugation, and recovering the lower phase. Both extractions were combined. The chloroform was evaporated using $N_2$ gas while keeping the sample in a 37 °C block. Once all the solvent was evaporated, the lipids were resuspended in 200 μL of chloroform and stored at −80 °C for subsequent analysis.

Analysis of lipids, including neutral (DAGs and TAGs) and polar lipids (PC, PE, PI, PG, MGDG, and DGDG) were carried out using high-resolution/accurate mass (HR/AM) lipidomics with a Vanquish–Q Exactive Plus UPLC-MS/MS system (Thermo Fisher Scientific). Although TAGs were measured and are included in the *SI Appendix*, Table S1, they have been excluded from the percentage calculations in Fig. 3 and *SI Appendix*, Fig. S11 to facilitate data analysis. The analytical protocol is based on the publication by Bird et al. (91) with some modifications. Briefly, 10 μL total lipid extract was injected into the UPLC/MS (Thermo Vanquish system). Separation occurred on a Thermo Scientific Accucore C18 column (2.1 × 150 mm, 2.6 mm) at 35 oC, with the autosampler tray temperature set at 10 °C and a flow rate of 400 μL $min^{-1}$. The mobile phase consisted of A: 10 mM ammonium formate in 50% acetonitrile plus 0.1% formic acid and B: 2 mM ammonium formate in acetonitrile/propan-2-ol/water 10/88/2 plus 0.02% formic acid. The elution gradient spanned 28 min, starting at 35% B and reaching 100% at 24 min.

The Thermo Q Exactive HESI II conditions utilized a sweep plate in the C probe position. Conditions were adjusted for separate positive and negative runs, with running samples in a single polarity resulting in more identifications. LC/MS was performed at 140 K resolution, and HCD MS2 experiments (35 K resolution) were conducted in positive and negative ion modes. Full scans were conducted at 140,000 resolution from m/z 150 to 1,200, followed by top 15 MS/MS at 35,000 resolution. The stepped collision energy was set at 25, 30, and 40, with the replacement of 25 with 30 in negative ion mode.

For positive ion mode, sheath gas was set to 60, Aux gas to 20, sweep gas to 1, and spray voltage to 3.2 KV with slight adjustments in negative ion mode. Capillary temperature was maintained at 320 oC, and the aux gas heater was set to 370 °C. Lipid search 5 by Thermo Fisher Scientific was used for lipid characterization. Potential lipid species were identified separately from positive or negative ion adducts. The data from each replicate were aligned within a chromatographic time window by combining positive and negative ion annotations, subsequently merged into a single lipid annotation. Identified lipid molecular species were quantified using polar and neutral lipid standards, 13:0-LPC, di24:1-PC, di14:0-PE, di18:0-PI, di14:0-PG, di18:0-PS, and di14:0-PA (supplied by Avanti Polar Lipids, USA), 0.857 nmol of tri15:0 TAG and 0.043 nmol 18:0-20:4 DAG (supplied by Nu-Chek-Prep). Full documentation of lipid profiling data is provided in Dataset S1.

**Cold Treatment for Root Cell Viability.** Six-day-old seedlings of WT, *syt1*, and *dgk1dgk2*, grown under standard conditions, were subjected to prechilled liquid 1/10 strength MS medium at 6 °C for 30 min. Following treatment, the seedlings were stained with a 1/10 MS solution containing 10 μg/mL FDA (Sigma; FDA stock solution at 5 mg/mL in DMSO) for 5 min. After staining, the seedlings were washed, and images were captured. Imaging for all roots was completed within 5 min. The experiment was repeated three times with consistent results.

**Freezing Assays.** Freezing tolerance assays were conducted on soil-grown plants in growth chambers at 20 °C under long-day conditions for 2 wk. For cold acclimation, the plants were transferred to growth chambers at 4 °C under long-day photoperiod with a light intensity of 40 μmol $m^{-2}$ $s^{-1}$ for 7 d. Freezing treatments were performed by keeping the plants at 4 °C for 1 h, after which the temperature was lowered (1 °C/30 min) until a temperature of −10 °C was reached. After 6 h at −10 °C, the temperature was elevated to 4 °C (1 °C/30 min). Subsequently, the plants were returned to growth chambers at 20 °C under long-day conditions, and after 1 wk of recovery, survival rates were assessed. Five biological replicates (>20 plants per replicate) were performed.

**Statistic and Graphs.** RNAseq overlap enrichment between *dgk1dgk2* and *syt1* and the associated *P*-value were calculated using the Web tool http://nemates.org/MA/progs/representation.stats.html. Enrichment was determined as the number of overlapping genes divided by the expected number of overlapping genes

from both groups, with expected genes calculated as (no. of genes in *dgk1dgk2* * no. of genes in *syt1*)/total genes analyzed in the genome.

Statistical analyses were performed using Prism 8.02 (GraphPad Software, www.graphpad.com), including unpaired *t* tests (*$P < 0.05$) and one-way or two-way ANOVA followed by Tukey's or Dunnett's multiple comparison test (**$P < 0.0001$; *$P < 0.0002$). Asterisks in figures indicate statistical differences between mutants and Col-0 or treatments and mock. Lowercase letters in graphs denote significant differences. Figure legends define "n" as the number of plants analyzed phenotypically or the number of ROIs analyzed for FRET quantification or ER–PM CS/ER ratio. Experiments were repeated at least three times with similar results. Graphs were mainly generated in Prism 8.02, and bubble plots in Prism 9.00.

**Accession Numbers.** The genes investigated in this research are cataloged publicly in The *Arabidopsis* Information Resource (https://www.arabidopsis.org/) with the corresponding accession numbers: *DGK1*: AT5G07920; *DGK2*: AT5G63770; *DGK3*: AT2G18730; *DGK4*: AT5G57690; *DGK5*: AT2G20900; *DGK6*: AT4G28130; *DGK7*: AT4G30340; *SYT1*: AT2G20990.

**Data, Materials, and Software Availability.** RNAseq data have been deposited in NCBI GEO SRA (Sequence Read Archive) (SUB15096052) with open access (92). The genes investigated in this research are cataloged publicly in The *Arabidopsis* Information Resource (https://www.arabidopsis.org/) with the corresponding accession numbers: *DGK1*: AT5G07920; *DGK2*: AT5G63770; *DGK3*: AT2G18730; *DGK4*: AT5G57690; *DGK5*: AT2G20900; *DGK6*: AT4G28130; *DGK7*: AT4G30340; *SYT1*: AT2G20990.

**ACKNOWLEDGMENTS.** We would like to thank the Interactomics Facility of the VIB department PLant Systems Biology for the Turbo-ID collaboration. We acknowledge Alicia Esteban del Valle for confocal images assistance, and Tabata Rosas for providing the FRET protocol, both from IHSM-CSIC-UMA (Instituto de Hortofruticultura Subtropical y Mediterránea, Málaga, Spain). We also thank Susana Silvestre from Rothamsted Research for helping in the management of sending samples. We appreciate the equipment provided by Remedios Crespillo and the SCAI Facility at the University of Málaga. The ER marker was a gift from Iraida Amaya Saavedra (IFAPA-Centro de Churriana, Málaga, Spain). We thank Plan Propio from the University of Málaga for financial support. M.A.B. was funded by the Spanish Ministry for Science and Innovation (grant no. PID2020-114419RB-I00 and PID2023-147983OB-I00) and by the Junta de Andalucia PAIDI 2020-PY20-00084. S.G.-H. was financed by the Researcher Training Fellowship, FPI, from the Ministry for Science and Innovation (PRE2018-085284). This work was supported by the Ministry for Science and Innovation (PID2021-127649OB-I00 to N.R.-L.) and by the Junta de Andalucía (PAIDI2020-P20-00222-R to N.R.-L.). V.A.-S. was supported by an Emerging Investigator research project (UMA20- FEDERJA-007), cofinanced by the "Programa Operativo FEDER 2014-2020" and by the "Consejería de Economía y Conocimiento de la Junta de Andalucía." Y.J. has received funding from the European Research Council under the European Union's Horizon 2020 research and innovation program (Grant Agreement No 101001097), and V.M. is supported by a long-term postdoctoral fellowship from the European Molecular Biology Organization (Grant Agreement ALTF 466-2022). Work by R.H., L.M., and J.N. was supported by a BBSRC (UK) Institute Strategic Program Grant (Green Engineering, BB/X010988/1). J.P.-S. and R.C. were funded by the Spanish Ministry for Science and Innovation (PID2019-106987RB-I00).

Author affiliations: [a]Área de Mejora y Fisiología de Plantas. Instituto de Hortofruticultura Subtropical y Mediterránea "La Mayora", Universidad de Málaga-Consejo Superior de Investigaciones Científicas, Málaga 29010, Spain; [b]Rothamsted Research, Harpenden AL5 2JQ, United Kingdom; [c]Departamento de Biotecnología Microbiana y de Plantas, Centro de Investigaciones Biológicas Margarita Salas-Consejo Superior de Investigaciones Científicas, Madrid 28040, Spain; and [d]Laboratoire Reproduction et Developpement des Plantes, Ecole Normale Supérieure de Lyon de Lyon, CNRS, INRAe, Lyon 69364, France

1. R. Fernández-Busnadiego, Y. Saheki, P. De Camilli, Three-dimensional architecture of extended synaptotagmin-mediated endoplasmic reticulum-plasma membrane contact sites. *Proc. Natl. Acad. Sci. U.S.A.* **112**, E2004–E2013 (2015).
2. Y. Jaillais *et al.*, Guidelines for naming and studying plasma membrane domains in plants. *Nat. Plants* **10**, 1172–1183 (2024).
3. M. Eisenberg-Bord *et al.*, CNM1 mediates nucleus–mitochondria contact site formation in response to phospholipid levels. *J. Cell Biol.* **220**, e202104100 (2021).
4. J. Pérez-Sancho *et al.*, Stitching organelles: Organization and function of specialized membrane contact sites in plants. *Trends Cell Biol.* **26**, 705–717 (2016).
5. C. L. Chang *et al.*, Feedback regulation of receptor-induced $Ca^{2+}$ signaling mediated by E-SYT1 and NIR2 at endoplasmic reticulum-plasma membrane junctions. *Cell Rep.* **5**, 813–825 (2013).
6. M. J. Phillips, G. K. Voeltz, Structure and function of ER membrane contact sites with other organelles. *Nat. Rev. Mol. Cell Biol.* **17**, 69–82 (2016).
7. W. A. Prinz, Bridging the gap: Membrane contact sites in signaling, metabolism, and organelle dynamics. *J. Cell Biol.* **205**, 759–769 (2014).
8. E. M. Bayer, I. Sparkes, S. Vanneste, A. Rosado, From shaping organelles to signaling platforms: The emerging functions of plant ER–PM contact sites. *Curr. Opin. Plant Biol.* **40**, 89–96 (2017).
9. L. Scorrano *et al.*, Coming together to define membrane contact sites. *Nat. Commun.* **10**, 1–11 (2019).
10. H. Wu, P. Carvalho, G. K. Voeltz, Here, there, and everywhere: The importance of ER membrane contact sites. *Science* **361**, 466 (2018).
11. Y. Saheki *et al.*, Control of plasma membrane lipid homeostasis by the extended synaptotagmins. *Nat. Cell Biol.* **18**, 504–515 (2016).
12. Y. Saheki, P. De Camilli, Endoplasmic reticulum–Plasma membrane contact sites. *Annu. Rev. Biochem.* **86**, 659–84 (2017).
13. W. Siao, P. Wang, B. Voigt, P. J. Hussey, F. Baluska, Arabidopsis SYT1 maintains stability of cortical endoplasmic reticulum networks and VAP27-1-enriched endoplasmic reticulum-plasma membrane contact sites. *J. Exp. Bot.* **67**, 6161–6171 (2016).
14. K. O. Kopec, V. Alva, A. N. Lupas, Homology of SMP domains to the TULIP superfamily of lipid-binding proteins provides a structural basis for lipid exchange between ER and mitochondria. *Bioinformatics* **26**, 1927–1931 (2010).
15. N. Ruiz-Lopez *et al.*, Synaptotagmins at the endoplasmic reticulum–plasma membrane contact sites maintain diacylglycerol homeostasis during abiotic stress. *Plant Cell* **33**, 2431–2453 (2021).
16. C. M. Schauder *et al.*, Structure of a lipid-bound extended synaptotagmin indicates a role in lipid transfer. *Nature* **510**, 552–555 (2014).
17. S. García-Hernández *et al.*, Functional and structural analysis reveals distinct biological roles of plant synaptotagmins in response to environmental stress. *Plant Cell Environ.* **48**, 260–271 (2025).
18. J. Pérez-Sancho *et al.*, The Arabidopsis synaptotagmin1 is enriched in endoplasmic reticulum-plasma membrane contact sites and confers cellular resistance to mechanical stresses. *Plant Physiol.* **168**, 132–143 (2015).
19. A. L. Schapire *et al.*, Arabidopsis synaptotagmin 1 is required for the maintenance of plasma membrane integrity and cell viability. *Plant Cell* **20**, 3374–3388 (2008).
20. S. A. Arisz *et al.*, Rapid phosphatidic acid accumulation in response to low temperature stress in Arabidopsis is generated through diacylglycerol kinase. *Front. Plant Sci.* **4**, 1–15 (2013).
21. K. Kanehara *et al.*, Arabidopsis AtPLC2 is a primary phosphoinositide-specific phospholipase C in phosphoinositide metabolism and the endoplasmic reticulum stress response. *PLoS Genet.* **11**, 1–19 (2015).
22. L. Kong *et al.*, Dual phosphorylation of DGK5-mediated PA burst regulates ROS in plant immunity. *Cell* **187**, 609–623.e21 (2024).
23. I. Pokotylo, V. Kravets, J. Martinec, E. Ruelland, The phosphatidic acid paradox: Too many actions for one molecule class? *Prog. Lipid Res.* **71**, 43–53 (2018).
24. P. Campomanes, V. Zoni, S. Vanni, Local accumulation of diacylglycerol alters membrane properties nonlinearly due to its transbilayer activity. *Commun. Chem.* **2**, 1–8 (2019).
25. N. Gaude, C. Bréhélin, G. Tischendorf, F. Kessler, P. Dörmann, Nitrogen deficiency in Arabidopsis affects galactolipid composition and gene expression and results in accumulation of fatty acid phytyl esters. *Plant J.* **49**, 729–739 (2007).
26. I. C. K. Foka *et al.*, The emerging roles of diacylglycerol kinase (DGK) in plant stress tolerance, growth, and development. *Agronomy* **10**, 1375 (2020).
27. M. N. Vaultier *et al.*, The hydrophobic segment of Arabidopsis thaliana cluster I diacylglycerol kinases is sufficient to target the proteins to cell membranes. *FEBS Lett.* **582**, 1743–1748 (2008).
28. A. E. Angkawijaya, V. C. Nguyen, F. Gunawan, Y. Nakamura, A pair of Arabidopsis diacylglycerol kinases essential for gametogenesis and endoplasmic reticulum phospholipid metabolism in leaves and flowers. *Plant Cell* **32**, 2602–2620 (2020).
29. F. Sakane, S.-I. Imai, M. Kai, S. Yasuda, H. Kanoh, Diacylglycerol kinases: Why so many of them? *Biochim. Biophys. Acta* **1771**, 793–806 (2007).
30. S. Xie, N. Naslavsky, S. Caplan, Diacylglycerol kinases in membrane trafficking. *Cell Logist.* **5**, e1078431 (2015).
31. N. Kobayashi *et al.*, Differential subcellular targeting and activity-dependent subcellular localization of diacylglycerol kinase isozymes in transfected cells. *Eur. J. Cell Biol.* **86**, 433–444 (2007).
32. J. C. Bozelli, R. M. Epand, Role of membrane shape in regulating the phosphatidylinositol cycle at contact sites. *Chem. Phys. Lipids* **221**, 24–29 (2019).
33. Y. J. Chen, C. G. Quintanilla, J. Liou, Recent insights into mammalian ER–PM junctions. *Curr. Opin. Cell Biol.* **57**, 99–105 (2019).
34. F. Lin *et al.*, Emerging roles of phosphoinositide-associated membrane trafficking in plant stress responses. *J. Genet. Genomics* **49**, 726–734 (2022).
35. S. A. Arisz, C. Testerink, T. Munnik, Plant PA signaling via diacylglycerol kinase. *Biochim. Biophys. Acta* **1791**, 869–875 (2009).
36. T. Kalachova *et al.*, Diacylglycerol kinase 5 participates in flagellin-induced signaling in Arabidopsis. *Plant Physiol.* **190**, 1978–1996 (2022).
37. K. Ishikawa, K. Tamura, Y. Fukao, T. Shimada, Structural and functional relationships between plasmodesmata and plant endoplasmic reticulum–plasma membrane contact sites consisting of three synaptotagmins. *New Phytol.* **226**, 798–808 (2020).
38. E. Lee *et al.*, Rare earth elements induce cytoskeleton-dependent and PI4P-associated rearrangement of SYT1/SYT5 endoplasmic reticulum-plasma membrane contact site complexes in Arabidopsis. *J. Exp. Bot.* **71**, 3986–3998 (2020).
39. V. Kriechbaumer *et al.*, Reticulomics: Protein-protein interaction studies with two plasmodesmata-localized reticulon family proteins identify binding partners enriched at plasmodesmata, endoplasmic reticulum, and the plasma membrane. *Plant Physiol.* **169**, 1933–1945 (2015).

40. F. C. Gómez-Merino, P. Pérez-Rodríguez, J. V. Hidalgo-Contreras, L. I. Trejo-Téllez, H. F. Escobar-Sepúlveda, Diacylglycerol kinases are widespread in higher plants and display inducible gene expression in response to beneficial elements, metal, and metalloid ions. *Front. Plant Sci.* **8**, 1–16 (2017).
41. F. C. Gómez-Merino, B. Mueller-Roeber, M.-I. Zanor, AtDGK2, a novel diacylglycerol kinase from Arabidopsis thaliana, phosphorylates 1-stearoyl-2-arachidonoyl-sn-glycerol and 1,2-dioleoyl-sn-glycerol and exhibits cold-inducible gene expression. *J. Biol. Chem.* **279**, 8230–8241 (2004).
42. F. Colón-González, M. G. Kazanietz, C1 domains exposed: From diacylglycerol binding to protein-protein interactions. *Biochim. Biophys. Acta* **1761**, 827–837 (2006).
43. N. Anilkumar, M. Parsons, R. Monk, T. Ng, J. C. Adams, Interaction of fascin and protein kinase Cα: A novel intersection in cell adhesion and motility. *EMBO J.* **22**, 5390–5402 (2003).
44. E. Lee *et al.*, Ionic stress enhances ER–PM connectivity via phosphoinositide-associated SYT1 contact site expansion in Arabidopsis. *Proc. Natl. Acad. Sci. U.S.A.* **116**, 1420–1429 (2019).
45. C. Sommer, C. Straehle, U. Kothe, F. A. Hamprecht, "Ilastik: Interactive learning and segmentation toolkit" in *Proceedings–International Symposium on Biomedical Imaging* (2011), pp. 230–233, 10.1109/ISBI.2011.5872394.
46. M. L. A. Simon *et al.*, A PtdIns(4)P-driven electrostatic field controls cell membrane identity and signaling in plants. *Nat. Plants* **2**, 1–10 (2016).
47. C. Vergnolle *et al.*, The cold-induced early activation of phospholipase C and D pathways determines the response of two distinct clusters of genes in Arabidopsis cell suspensions. *Plant Physiol.* **139**, 1217–1233 (2005).
48. A. Levy, J. Y. Zheng, S. G. Lazarowitz, Synaptotagmin SYTA forms ER-plasma membrane junctions that are recruited to plasmodesmata for plant virus movement. *Curr. Biol.* **25**, 2018–2025 (2015).
49. J. D. Lewis, S. G. Lazarowitz, Arabidopsis synaptotagmin SYTA regulates endocytosis and virus movement protein cell-to-cell transport. *Proc. Natl. Acad. Sci. U.S.A.* **107**, 2491–2496 (2010).
50. A. Uchiyama *et al.*, The Arabidopsis synaptotagmin SYTA regulates the cell-to-cell movement of diverse plant viruses. *Front. Plant Sci.* **5**, 1–17 (2014).
51. H. Kim *et al.*, Synaptotagmin 1 negatively controls the two distinct immune secretory pathways to powdery mildew fungi in Arabidopsis. *Plant Cell Physiol.* **57**, 1133–1141 (2016).
52. M. F. Thomashow, Plant cold acclimation: Freezing tolerance genes and regulatory mechanisms. *Annu. Rev. Plant Biol.* **50**, 571–599 (1999).
53. M. K. Topham, R. M. Epand, Mammalian diacylglycerol kinases: Molecular interactions and biological functions of selected isoforms. *Biochim. Biophys. Acta* **1790**, 416–424 (2009).
54. Y. Yakubchyk *et al.*, Regulation of neurite outgrowth in N1E–115 cells through PDZ-mediated recruitment of diacylglycerol kinase ζ. *Mol. Cell Biol.* **25**, 7289–7302 (2005).
55. C. D. Nelson *et al.*, Targeting of diacylglycerol receptors by b-arrestins. *Science* **315**, 663–666 (2007).
56. J. C. Bozelli *et al.*, Human diacylglycerol kinase ϵ N-terminal segment regulates the phosphatidylinositol cycle, controlling the rate but not the acyl chain composition of its lipid intermediates. *ACS Chem. Biol.* **17**, 2495–2506 (2022).
57. J. C. Bozelli *et al.*, Membrane curvature allosterically regulates the phosphatidylinositol cycle, controlling its rate and acyl-chain composition of its lipid intermediates. *J. Biol. Chem.* **293**, 17780–17791 (2018).
58. J. H. Tao-Cheng, Activity-dependent decrease in contact areas between subsurface cisterns and plasma membrane of hippocampal neurons. *Mol. Brain* **11**, 1–8 (2018).
59. N. J. Blunsom, S. Cockcroft, Phosphatidylinositol synthesis at the endoplasmic reticulum. *Biochim. Biophys. Acta* **1865**, 158471 (2020).
60. C. L. Chang, Y. J. Chen, J. Liou, ER–plasma membrane junctions: Why and how do we study them? *Biochim. Biophys. Acta* **1864**, 1494–1506 (2017).
61. M. Kraub, V. Haucke, Directing lipid transport at membrane contact sites. *Nat. Cell Biol.* **18**, 461–463 (2016).
62. B. Xie, P. M. Nguyen, O. Idevall-Hagren, Feedback regulation of insulin secretion by extended synaptotagmin-1. *FASEB J.* **33**, 4716–4728 (2019).
63. J. A. Lees *et al.*, Lipid transport by TMEM24 at ER-plasma membrane contacts regulates pulsatile insulin secretion. *Science* **355**, 709 (2017).
64. E. W. Sun *et al.*, Lipid transporter TMEM24/C2CD2L is a $Ca^{2+}$-regulated component of ER–plasma membrane contacts in mammalian neurons. *Proc. Natl. Acad. Sci. U.S.A.* **116**, 5775–5784 (2019).
65. B. Xie *et al.*, The endoplasmic reticulum–plasma membrane tethering protein TMEM24 is a regulator of cellular Ca2+ homeostasis. *J. Cell Sci.* **135**, 1–14 (2022).
66. Y. J. Kim, M. L. Guzman-Hernandez, E. Wisniewski, N. Echeverria, T. Balla, Phosphatidylinositol and phosphatidic acid transport between the ER and plasma membrane during PLC activation requires the Nir2 protein. *Biochem. Soc. Trans.* **44**, 197–201 (2016).
67. C. Löfke, T. Ischebeck, S. König, S. Freitag, I. Heilmann, Alternative metabolic fates of phosphatidylinositol produced by phosphatidylinositol synthase isoforms in Arabidopsis thaliana. *Biochem. J.* **413**, 115–124 (2008).
68. M. Karimi, A. Depicker, P. Hilson, Recombinational cloning with plant gateway vectors. *Plant Physiol.* **145**, 1144–1154 (2007).
69. J. Alassimone *et al.*, Polarly localized kinase SGN1 is required for Casparian strip integrity and positioning. *Nat. Plants* **2**, 16113 (2016).
70. J. F. Sánchez-Sevilla, E. Cruz-Rus, V. Valpuesta, M. A. Botella, I. Amaya, Deciphering gamma-decalactone biosynthesis in strawberry fruit using a combination of genetic mapping, RNA-Seq and eQTL analyses. *BMC Genomics* **15** (2014).
71. A. Lampropoulos *et al.*, GreenGate–A novel, versatile, and efficient cloning system for plant transgenesis. *PLoS One* **8**, e83043 (2013).
72. D. Arora *et al.*, Establishment of proximity-dependent biotinylation approaches in different plant model systems. *Plant Cell* **32**, 3388–3407 (2020).
73. A. Sullivan *et al.*, An 'eFP-Seq Browser' for visualizing and exploring RNA sequencing data. *Plant J.* **100**, 641–654 (2019).
74. D. Winter *et al.*, An "electronic fluorescent pictograph" browser for exploring and analyzing large-scale biological data sets. *PLoS One* **2**, 1–12 (2007).
75. T. Paysan-Lafosse *et al.*, InterPro in 2022. *Nucleic Acids Res.* **51**, D418–D427 (2023).
76. J. Jumper *et al.*, Highly accurate protein structure prediction with AlphaFold. *Nature* **596**, 583–589 (2021).
77. M. Varadi *et al.*, AlphaFold protein structure database: Massively expanding the structural coverage of protein-sequence space with high-accuracy models. *Nucleic Acids Res.* **50**, D439–D444 (2022).
78. J. Schindelin *et al.*, Fiji: An open-source platform for biological-image analysis. *Nat. Methods* **9**, 676–682 (2012).
79. C. Gehl, R. Waadt, J. Kudla, R. R. Mendel, R. Hänsch, New GATEWAY vectors for high throughput analyses of protein-protein interactions by bimolecular fluorescence complementation. *Mol. Plant* **2**, 1051–1058 (2009).
80. X. Liao, B. Zhang, M. R. Blatt, B. Zhang, A FRET method for investigating dimer/monomer status and conformation of the UVR8 photoreceptor. *Photochem. Photobiol. Sci.* **18**, 367–374 (2019).
81. V. Amorim-Silva *et al.*, TTL proteins scaffold brassinosteroid signaling components at the plasma membrane to optimize signal transduction in Arabidopsis. *Plant Cell* **31**, 1807–1828 (2019).
82. S. Kumar, G. Stecher, M. Li, C. Knyaz, K. Tamura, MEGA X: Molecular evolutionary genetics analysis across computing platforms. *Mol. Biol. Evol.* **35**, 1547–1549 (2018).
83. A. M. Bolger, M. Lohse, B. Usadel, Trimmomatic: A flexible trimmer for Illumina sequence data. *Bioinformatics* **30**, 2114–2120 (2014).
84. D. Kim, B. Langmead, S. L. Salzberg, HISAT: A fast spliced aligner with low memory requirements. *Nat. Methods* **12**, 357–360 (2015).
85. C. Trapnell *et al.*, Differential analysis of gene regulation at transcript resolution with RNA-seq. *Nat. Biotechnol.* **31**, 46–53 (2013).
86. I. Milne *et al.*, Using Tablet for visual exploration of second-generation sequencing data. *Brief Bioinform.* **14**, 193–202 (2013).
87. L. A. Goff, C. Trapnell, D. Kelley, CummeRbund: Visualization and Exploration of Cufflinks High-Throughput Sequencing Data (R Package Version 2, 2014), pp. 1–45.
88. P. D. Thomas *et al.*, PANTHER: Making genome-scale phylogenetics accessible to all. *Protein Sci.* **31**, 8–22 (2022).
89. K. Bernfur, O. Larsson, C. Larsson, N. Gustavsson, Relative abundance of integral plasma membrane proteins in Arabidopsis leaf and root tissue determined by metabolic labeling and mass spectrometry. *PLoS One* **8**, e71206 (2013).
90. C. Larsson, M. Sommarin, S. Widell, Isolation of highly purified plant plasma membranes and separation of inside-out and right-side-out vesicles. *Methods* **228**, 1994 (1994).
91. S. S. Bird, V. R. Marur, M. J. Sniatynski, H. K. Greenberg, S. Bruce, Lipidomics profiling by high resolution LC-MS and HCD fragmentation: Focus on characterization of mitochondrial cardiolipins and monolysocardiolipins. *Anal. Chem.* **83**, 940–949 (2012).
92. M. A. Botella, S. Garcia-Hernandez, Sequential coupling of synaptotagmins and diacylglycerol kinases synergistically regulates diacylglycerol metabolism at ER-PM contact sites. Gene Expression Omnibus. https://www.ncbi.nlm.nih.gov/geo/query/acc.cgi. Deposited 1 February 2025.